

Projectile Roll Dynamics and Control With a Low-Cost Skid-to-Turn Maneuver System

by Frank Fresconi, Ilmars Celmins, Mark Ilg, and James Maley

ARL-TR-6363

March 2013

NOTICES

Disclaimers

The findings in this report are not to be construed as an official Department of the Army position unless so designated by other authorized documents.

Citation of manufacturer's or trade names does not constitute an official endorsement or approval of the use thereof.

Destroy this report when it is no longer needed. Do not return it to the originator.

Army Research Laboratory

Aberdeen Proving Ground, MD 21005-5069

ARL-TR-6363**March 2013**

Projectile Roll Dynamics and Control With a Low-Cost Skid-to-Turn Maneuver System

Frank Fresconi, Ilmars Celmins, Mark Ilg, and James Maley
Weapons and Materials Research Directorate, ARL

REPORT DOCUMENTATION PAGE				Form Approved OMB No. 0704-0188	
Public reporting burden for this collection of information is estimated to average 1 hour per response, including the time for reviewing instructions, searching existing data sources, gathering and maintaining the data needed, and completing and reviewing the collection information. Send comments regarding this burden estimate or any other aspect of this collection of information, including suggestions for reducing the burden, to Department of Defense, Washington Headquarters Services, Directorate for Information Operations and Reports (0704-0188), 1215 Jefferson Davis Highway, Suite 1204, Arlington, VA 22202-4302. Respondents should be aware that notwithstanding any other provision of law, no person shall be subject to any penalty for failing to comply with a collection of information if it does not display a currently valid OMB control number. PLEASE DO NOT RETURN YOUR FORM TO THE ABOVE ADDRESS.					
1. REPORT DATE (DD-MM-YYYY) March 2013		2. REPORT TYPE Final		3. DATES COVERED (From - To) October 2011–September 2012	
4. TITLE AND SUBTITLE Projectile Roll Dynamics and Control With a Low-Cost Skid-to-Turn Maneuver System				5a. CONTRACT NUMBER	
				5b. GRANT NUMBER	
				5c. PROGRAM ELEMENT NUMBER	
6. AUTHOR(S) Frank Fresconi, Ilmars Celmins, Mark Ilg, and James Maley				5d. PROJECT NUMBER AH80	
				5e. TASK NUMBER	
				5f. WORK UNIT NUMBER	
7. PERFORMING ORGANIZATION NAME(S) AND ADDRESS(ES) U.S. Army Research Laboratory ATTN: RDRL-WML-E Aberdeen Proving Ground, MD 21005-5066				8. PERFORMING ORGANIZATION REPORT NUMBER ARL-TR-6363	
9. SPONSORING/MONITORING AGENCY NAME(S) AND ADDRESS(ES)				10. SPONSOR/MONITOR'S ACRONYM(S)	
				11. SPONSOR/MONITOR'S REPORT NUMBER(S)	
12. DISTRIBUTION/AVAILABILITY STATEMENT Approved for public release; distribution is unlimited.					
13. SUPPLEMENTARY NOTES					
14. ABSTRACT A low-cost maneuver control system was successfully developed to provide enhanced maneuverability of gun-launched munitions. The unique environment and aspects of the system are described. Electromechanical design of the maneuver system was undertaken. Laboratory experiments were conducted to ensure survivability at gun launch and characterize the response. Aerodynamics and flight mechanics of the projectile roll behavior and actuator dynamics were formulated. These nonlinear dynamics were expressed in a linear state-space model for controllability, control design, and stability analysis. Roll response was investigated through nonlinear simulation and wind tunnel experiments. Monte Carlo simulations illustrate suitable performance of the maneuver control system. Experiments further validate the unique projectile maneuver technology and approach, reveal nonideal characteristics of the system, and verify modeling and simulation.					
15. SUBJECT TERMS projectile, maneuver, flight control, roll					
16. SECURITY CLASSIFICATION OF:			17. LIMITATION OF ABSTRACT UU	18. NUMBER OF PAGES 54	19a. NAME OF RESPONSIBLE PERSON Frank Fresconi
a. REPORT Unclassified	b. ABSTRACT Unclassified	c. THIS PAGE Unclassified			19b. TELEPHONE NUMBER (Include area code) 410-306-0794

Contents

List of Figures	v
List of Tables	vii
1. Introduction	1
2. Low-Cost, Gun-Hard Skid-to-Turn Maneuver System	2
2.1 Maneuver System Design.....	2
2.2 Experimental Characterization	3
2.2.1 Shock	3
2.2.2 Response.....	4
3. Dynamics	5
3.1 Projectile Roll Dynamics.....	5
3.2 Actuator Dynamics.....	6
4. Control Technique	6
4.1 State Space Formulation and Controllability	6
4.2 Linear Quadratic Regulator Algorithm	7
4.3 Stability Analysis	8
5. Simulation Setup	10
6. Experimental Setup	11
6.1 Airframe, Instrumentation, and Wind Tunnel Facility	11
6.2 Procedure.....	13
7. Results	13
7.1 Nonlinear Simulation	13
7.2 Experiment	20
8. Conclusions	34

9. References	36
Nomenclature	39
Distribution List	41

List of Figures

Figure 1. Solid model rendering of maneuver system (left) utilizing COTS servomechanism (right).	3
Figure 2. Maneuver system in shock facility.	4
Figure 3. Representative servomechanism in assembly command and response without aerodynamic loading.	5
Figure 4. System eigenvalues.	8
Figure 5. Root locus.	9
Figure 6. Bode diagram.	10
Figure 7. Model mounted in wind tunnel with high-speed camera and telemetry data acquisition.	12
Figure 8. Representative wind tunnel profile.	13
Figure 9. Nominal controlled response without fin cant at zero angle of attack and 10-Hz initial roll rate – roll angle.	14
Figure 10. Nominal controlled response without fin cant at zero angle of attack and 10-Hz initial roll rate – roll rate.	14
Figure 11. Nominal controlled response without fin cant at zero angle of attack and 10-Hz initial roll rate – deflections.	15
Figure 12. Monte Carlo controlled response without fin cant at zero angle of attack and 10-Hz initial roll rate – modulo roll angle histogram at 2 s.	16
Figure 13. Monte Carlo controlled response without fin cant at zero angle of attack and 10-Hz initial roll rate – roll rate.	17
Figure 14. Monte Carlo controlled response without fin cant at zero angle of attack and 10 Hz initial roll rate – deflections.	17
Figure 15. Monte Carlo controlled response with 2° fin cant at zero angle of attack and 10-Hz initial roll rate – modulo roll angle histogram at 2 s.	18
Figure 16. Monte Carlo controlled response with 2° fin cant at zero angle of attack and 10-Hz initial roll rate – roll rate.	19
Figure 17. Monte Carlo controlled response with 2° fin cant at zero angle of attack and 10-Hz initial roll rate – deflections.	19
Figure 18. Individual canard impulse response without fin cant at zero angle of attack – roll rate.	20
Figure 19. Individual canard impulse response without fin cant at zero angle of attack – deflections.	21
Figure 20. Group canard impulse response with 2° fin cant at zero angle of attack – roll rate.	22

Figure 21. Group canard impulse response with 2° fin cant at zero angle of attack – deflections.	22
Figure 22. Monte Carlo simulation and experimental controlled response without fin cant at zero angle of attack at 10 Hz initial roll rate – roll rate.	23
Figure 23. Monte Carlo simulation and experimental controlled response without fin cant at zero angle of attack at 10 Hz initial roll rate – deflections.	24
Figure 24. Controlled response without fin cant at zero angle of attack at 10-Hz initial roll rate – roll angle.	25
Figure 25. Controlled response without fin cant at zero angle of attack at 10-Hz initial roll rate – roll rate.	25
Figure 26. Controlled response without fin cant at zero angle of attack at 10-Hz initial roll rate – deflections.	26
Figure 27. Controlled response with 2° fin cant at zero angle of attack at 10-Hz initial roll rate – roll angle.	27
Figure 28. Controlled response with 2° fin cant at zero angle of attack at 10-Hz initial roll rate – roll rate.	27
Figure 29. Controlled response with 2° fin cant at zero angle of attack at 10-Hz initial roll rate – deflections.	28
Figure 30. Controlled response with 2° fin cant at zero angle of attack at 2-Hz initial roll rate – roll angle.	29
Figure 31. Controlled response with 2° fin cant at zero angle of attack at 2-Hz initial roll rate – roll rate.	29
Figure 32. Controlled response with 2° fin cant at zero angle of attack at 2-Hz initial roll rate – deflections.	30
Figure 33. Controlled response without fin cant at 5° angle of attack at 10-Hz initial roll rate – roll angle.	31
Figure 34. Controlled response without fin cant at 5° angle of attack at 10-Hz initial roll rate – roll rate.	31
Figure 35. Controlled response without fin cant at 5° angle of attack at 10-Hz initial roll rate – deflections.	32
Figure 36. Controlled response with 2° fin cant at 5° angle of attack at 10-Hz initial roll rate – roll angle.	33
Figure 37. Controlled response with 2° fin cant at 5° angle of attack at 10-Hz initial roll rate – roll rate.	33
Figure 38. Controlled response with 2° fin cant at 5° angle of attack at 10-Hz initial roll rate – deflections.	34

List of Tables

Table 1. System properties.....	11
Table 2. System uncertainties (1 standard deviation).	11

INTENTIONALLY LEFT BLANK.

1. Introduction

The overarching motivation for this work is to provide capability for gun-launched munitions to engage targets that require high maneuverability. Past efforts resulted in precision indirect fire for stationary targets (1–5). This report represents a component of a program focused on general development of this enhanced maneuverability for application to relevant systems, such as artillery, mortars, and shoulder-launched munitions.

The approach to achieve a low-cost, gun-hard skid-to-turn maneuver control system outlined in this report is to leverage commercial off-the-shelf (COTS) technology for the high-G environment and develop control algorithms that rely on a high-fidelity characterization of the aerodynamics and flight mechanics. A variety of state-of-the-art actuation technologies (6–8) may be considered for this application. Servomechanisms used by hobbyists to fly remote-controlled aircraft are low cost because of the high-volume manufacturing. One outstanding question is whether these devices perform to the standard necessary for guided projectile applications. Components must withstand the high structural loadings during gun launch (9, 10). Hardening components, such as a COTS servomechanism for gun launch, consist of properly supporting structures, minimizing mass, and reducing the number of moving parts.

Projectile aerodynamics and flight dynamics can be well understood by applying mature computational and experimental methods developed specifically for projectiles. Computational fluid dynamics techniques have been applied to complex projectile aerodynamic phenomena with much success (11–14). Spark ranges, in existence since the 1940s, provide extremely accurate aerodynamic coefficients (15–17) due to the free-flight nature and motion measurement accuracy of the experiment. Experimental techniques have enjoyed recent advancement with the onboard sensor technique (18).

A canted fin-stabilized, canard-controlled projectile flying in a skid-to-turn configuration was selected based on past work (19), which complicates the aerodynamic characterization resulting from flow interactions (18, 20, 21). Packaging constraints for gun tube launch require deploying stabilizing and control surfaces. Spin induced by gun rifling or fin cant improves ballistic launch accuracy but requires a consideration of roll-yaw resonance (22) for portions of the flight. A rocket motor, used for most missiles, is not currently a part of this system, therefore only the gun propellant may be used to supply the dynamic pressure necessary for target engagements that require high maneuverability. The skid-to-turn configuration was chosen for the high bandwidth since the time of flight for some applications of interest may be only 1 s. Quantifying the flight dynamics of this complex system through computational and experimental techniques is essential to developing and implementing simple, effective control solutions.

Classical and modern control techniques have been applied to the roll control problem for missiles (23–26). Coupled roll-pitch-yaw control of bank- and skid-to-turn maneuver systems have also been considered (21, 27–29). The approach herein is to formulate these techniques in the simplest manner possible for the unique projectile environment by including effects like fin cant and canard-fin interactions. Additionally, flexible body dynamics for missiles have been shown in simulation to cause instability; however, these effects may be ignored for this application since the flight body has been hardened to withstand gun launch. While missiles often integrate high-performance gyroscopes given a transfer alignment at separation to determine roll feedback, the harsh gun launch environment precludes such an arrangement. Alternate solutions, based on low-cost magnetometer or thermopile measurements, have been formulated (30–33).

The goal of this report is to develop and demonstrate roll control performance of a low-cost, gun-hard skid-to-turn maneuver system. The contribution of this work lies in leveraging COTS devices to reduce cost, ensuring structural integrity, and using high-fidelity flight characterization methods in the control strategy for the gun launch environment. A wide variety of technical disciplines have been successfully synthesized to develop this technology using theory, nonlinear simulation, and experiment.

The low-cost, gun-hard maneuver control system design and experimental characterization is presented in this report. Next, the dynamics of the projectile flight and actuation are given along with the state space construction, controllability, control design, and stability analysis. Setup and results of the nonlinear simulations and wind tunnel experiments are provided, followed by summary findings and conclusions.

2. Low-Cost, Gun-Hard Skid-to-Turn Maneuver System

2.1 Maneuver System Design

A generic class of fin-stabilized, canard-controlled munitions in the 60- to 155-mm-diameter range (mortars, artillery, shoulder-launched munitions, air-dropped munitions, etc.) may utilize this maneuver control system technology. The mechanical design of the maneuver system internally mounted near the nose and an image of the COTS servomechanism (Hitec HS-5056MG) are shown in figure 1. Four servomechanisms are each connected through a pinned arm to a control surface. Proper design of this linkage provides the required deflections of the control surfaces. Mechanical limits of $\pm 10^\circ$ were placed on the deflections.

The servomechanism consists of potentiometer feedback, processor for a motor control algorithm, driving electronics, and a brushed DC motor. This closed system is driven by an outside pulse-width modulated (PWM) signal that prescribes the angle of the output shaft of the motor and operates at a rate of 50 Hz.

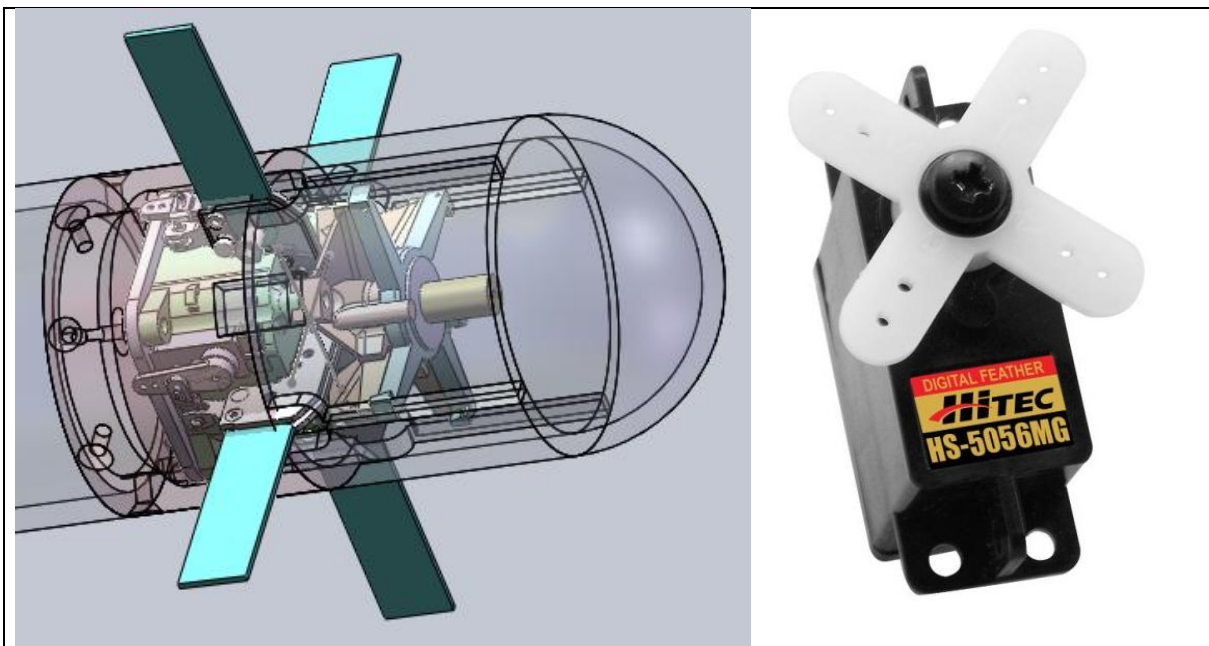


Figure 1. Solid model rendering of maneuver system (left) utilizing COTS servomechanism (right).

A digital signal processor (DSP) (Texas Instruments TMS320F28335) sends PWM commands to the servomechanism based on the embedded roll control algorithm. An analog-to-digital converter samples measurements for the roll feedback and potentiometer from each servomechanism. Diagnostics are also packaged on the DSP into a pulse-code modulated stream and sent to an S-band transmitter and antenna for data acquisition during experiments. Lithium ion batteries power the maneuver system.

As a cost reference point, components necessary for the present maneuver system are a couple hundred dollars, which is approximately a twofold decrease in the order of magnitude from some currently fielded precision munitions in relatively low volume (thousand units per year).

2.2 Experimental Characterization

2.2.1 Shock

Experiments were conducted to initially assess the survivability of the maneuver system during gun launch. Assemblies of the servomechanisms, housings, and linkages were built and tested for functionality by running the motors. These test articles were mounted as shown in figure 2 in a shock facility. The experimental shock setup is a plate instrumented with a reference accelerometer and the article under test, which is constrained to one-dimensional translation. The instrumented plate is accelerated from rest by releasing an elastic cable and undergoes a short period (usually order of <1 ms) of high acceleration at impact, which can be shaped by dampers.

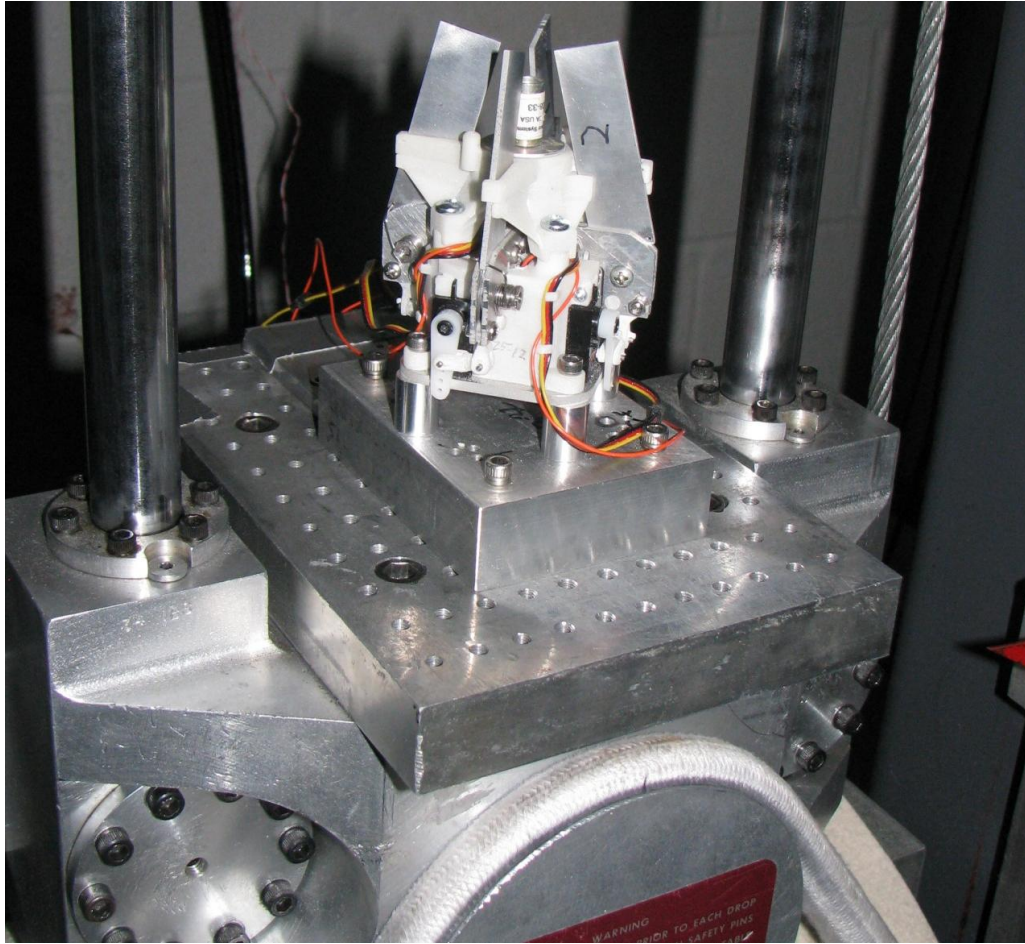


Figure 2. Maneuver system in shock facility.

The maneuver system was subjected to loadings up to 10,000 Gs. Post-shock inspection and functionality did not reveal any failures in the assembly. The acceleration limit for survivability was not found since the assemblies were tested successfully to 10,000 Gs (which is on the order of most mortar and artillery launches) and a specific gun-projectile combination were not of interest for this study.

2.2.2 Response

Simple experiments were performed on the bench in the laboratory on the maneuver system to identify salient features for modeling the system. Step commands in 1° increments from -9° to $+9^\circ$ were provided to each servomechanism, and the response was measured through the potentiometer. Calibrations were performed on an optical bench with a laser reflection measurement technique to relate potentiometer voltage to control surface deflection angle. An example of the step response is provided in figure 3. Analysis of these data illustrates that the significant actuator dynamics can be modeled as a first-order system with a delay. Major phenomena that these experiments do not capture are the aerodynamic loading and coupling of the projectile flight dynamics on the maneuver system.

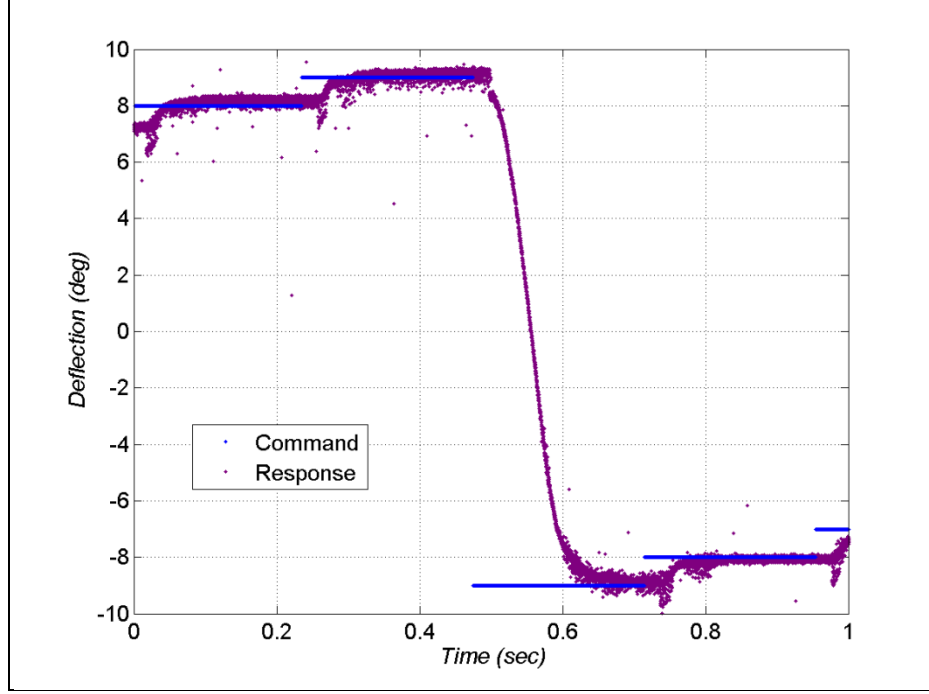


Figure 3. Representative servomechanism in assembly command and response without aerodynamic loading.

3. Dynamics

3.1 Projectile Roll Dynamics

Applying Newtonian kinetics yields the equation of motion for the projectile roll dynamics. The rate of change of the angular momentum is equal to the sum of the moments about the roll axis.

$$I_{xx}\ddot{\phi} = \bar{q}SD \left[\frac{DC_{lp}(M)}{2V} \dot{\phi} + \sum_{i=1}^{N_c} CP^R(M, \alpha_{c_i}) C_N^{c_i}(M, \alpha_{c_i}) + C_l(\delta_F, M, \bar{\alpha}, \phi_A, \delta_{c_i}) \right]. \quad (1)$$

Aerodynamic moments include static roll torque due to canted fins, deflected canards, and roll damping. Proper modeling and characterization of the aerodynamics are critical to developing a low-cost skid-to-turn maneuver system. The static roll torque coefficient is often a complex function of cant or bevel angle, Mach number, total angle of attack, aerodynamic roll angle, and canard deflection to account for the flow interactions of fins with the body and canards. Roll damping coefficient is a function of Mach number. Center-of-pressure (CP) of the canards can be a function of Mach number and angle of attack. Canard normal force coefficient is usually nonlinear with angle of attack and Mach number; the deflection angle is also sometimes used in the aerodynamic model. An odd-order Taylor series expansion up to the fifth order in angle of attack with look-up tables for the Mach variation models the canard normal force nonlinearities.

$$C_N^{C_i}(M, \alpha_{C_i}) = C_{N_\alpha}^C(M) \alpha_{C_i} + C_{N_{\alpha^3}}^C(M) \alpha_{C_i}^3 + C_{N_{\alpha^5}}^C(M) \alpha_{C_i}^5. \quad (2)$$

Here, the local angle of attack at each blade is a summation of the deflection angle and the flow velocity at each canard in the canard frame.

$$\alpha_{C_i} = \delta_{C_i} + \text{atan}\left(\frac{w_{C_i}}{u_{C_i}}\right). \quad (3)$$

Components of the flow velocity in the local canard frame are obtained by finding the velocity at each canard in the projectile body frame.

$$\vec{V}_{C_i/I}^B = \vec{V}_{CG/I} + \vec{\omega}_{B/I} \times \vec{r}_{CG \rightarrow CP_i}. \quad (4)$$

The transformation matrix from the projectile body frame to each canard frame is applied to calculate the velocity at each canard in the canard frame.

$$\vec{V}_{C_i/I}^{C_i} = \vec{T}_{B C_i} \vec{V}_{C_i/I}^B. \quad (5)$$

3.2 Actuator Dynamics

Inspection of the benchtop experimental response shows that the actuator dynamics can be described using a first-order system with a delay. Effects such as oscillation, overshoot, deadbanding, backlash, or hysteresis were not included. An open question that this research addresses is whether actuation technology shortfalls may be overcome through a systems approach. The model for the first-order system with time constant is given in the following equation. The time delay was incorporated by simply delaying the deflection commands by a prescribed amount of time.

$$\tau \dot{\delta} + \delta = \delta_{CMD}. \quad (6)$$

4. Control Technique

4.1 State Space Formulation and Controllability

The projectile roll and actuator dynamics can be packaged into a state space representation to apply an array of control techniques. The states for this problem are roll, roll rate, and the four canard deflections.

$$\vec{x} = [\phi \quad \dot{\phi} \quad \delta_{C_1} \quad \delta_{C_2} \quad \delta_{C_3} \quad \delta_{C_4}]^T. \quad (7)$$

The controls are the deflection commands for the four canards.

$$\vec{u} = [\delta_{C_1,CMD} \quad \delta_{C_2,CMD} \quad \delta_{C_3,CMD} \quad \delta_{C_4,CMD}]^T. \quad (8)$$

By linearizing the aerodynamic model and re-expressing the equations of motion, we obtained the system dynamics matrix.

$$\vec{A} = \begin{bmatrix} 0 & 1 & 0 & 0 & 0 & 0 \\ 0 & \frac{\bar{q}SD^2C_{lp}}{2VI_{XX}} & \frac{\bar{q}SDCP^RC_{N\alpha}^C}{I_{XX}} & \frac{\bar{q}SDCP^RC_{N\alpha}^C}{I_{XX}} & \frac{\bar{q}SDCP^RC_{N\alpha}^C}{I_{XX}} & \frac{\bar{q}SDCP^RC_{N\alpha}^C}{I_{XX}} \\ 0 & 0 & -\frac{1}{\tau_1} & 0 & 0 & 0 \\ 0 & 0 & 0 & -\frac{1}{\tau_2} & 0 & 0 \\ 0 & 0 & 0 & 0 & -\frac{1}{\tau_3} & 0 \\ 0 & 0 & 0 & 0 & 0 & -\frac{1}{\tau_4} \end{bmatrix}. \quad (9)$$

The time constant of each canard may be unique. The controls matrix has the following form.

$$\vec{B} = \begin{bmatrix} 0 & 0 & 0 & 0 \\ 0 & 0 & 0 & 0 \\ \frac{1}{\tau_1} & 0 & 0 & 0 \\ 0 & \frac{1}{\tau_2} & 0 & 0 \\ 0 & 0 & \frac{1}{\tau_3} & 0 \\ 0 & 0 & 0 & \frac{1}{\tau_4} \end{bmatrix}. \quad (10)$$

Additionally, the static roll torque adds a forcing function.

$$\vec{F} = \begin{bmatrix} 0 \\ \frac{qSDC_l}{I_{XX}} \\ 0 \\ 0 \\ 0 \\ 0 \end{bmatrix}. \quad (11)$$

The system is controllable, as the rank of the controllability matrix ($Co = [\vec{B} \ \vec{A}\vec{B} \ \vec{A}^2\vec{B} \ \vec{A}^3\vec{B} \ \vec{A}^4\vec{B} \ \vec{A}^5\vec{B}]$) is equal to the number of states.

4.2 Linear Quadratic Regulator Algorithm

The linear quadratic regulator expresses the control as $\vec{u} = -\vec{K}\vec{x}$. The weightings for control effort and control error enable proper tuning of the controller for a given application. The gain is given by the following expression.

$$\vec{K} = \vec{R}^{-1}\vec{B}^T\vec{P}. \quad (12)$$

The matrix \vec{P} is calculated by solving the matrix Riccati equation.

$$\vec{A}^T \vec{P} + \vec{P} \vec{A} - \vec{P} \vec{B} \vec{R}^{-1} \vec{B}^T \vec{P} + \vec{Q} = 0 . \quad (13)$$

The error signal used in the control law is formed by differencing the feedback from the desired states. The airframe flies in an “X” configuration for optimal maneuverability. For reasons of symmetry, the desired roll angle can be any of four locations, which are 90° apart in roll. A trapezoidal error signal was formed using these symmetry locations, and the roll feedback to drive the roll angle to the nearest symmetry location. Roll rate feedback was regulated to zero. While canard deflection feedback is available, after some analysis it was decided not to use this information for closed loop control for reasons of increased cost of calibration, processing, and reliability necessary for a sufficiently clean feedback signal. Additionally, feed forward gain may be used when fins are canted since the effectiveness of both the fins and canards and fin cant angle is known. Saturation occurred when the commands were greater than the mechanical limits of $\pm 10^\circ$.

4.3 Stability Analysis

The linear state space representation of the nonlinear projectile roll and actuator dynamics was used to conduct a stability analysis during control design. Recall that nonlinearities in the aerodynamics, actuator delay, and deflection limiter were ignored for this analysis.

Eigenvalues for roll and roll rate are presented in figure 4. The uncontrolled system has a marginally unstable eigenvalue. Comparing the uncontrolled and controlled cases shows that damping is increased and oscillations are induced for the controlled system.

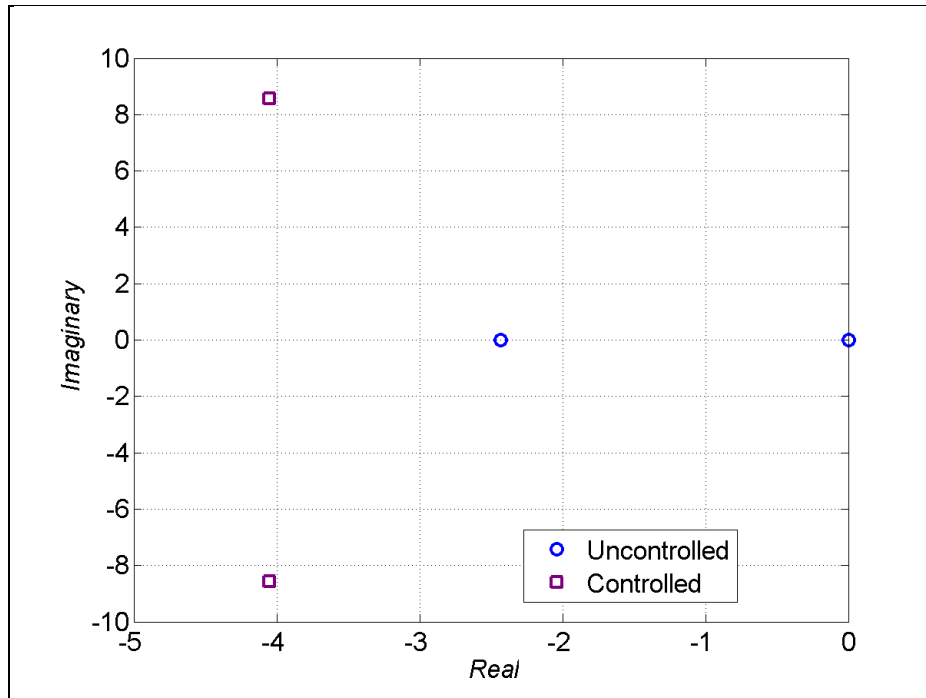


Figure 4. System eigenvalues.

The root locus analysis illustrates the behavior of the roll and roll rate as the control gain is changed. Figure 5 shows that the roll response increases in frequency as the gain increases. As gain increases to about 3, the rolling motion becomes unstable before again becoming stable at even higher values of gain (above 50). Roll rate stability increases as gain increases with a minor decrease in frequency. After a gain of about 0.05, the dominant roll rate mode shifts, and roll rate behavior is unstable for high gain.

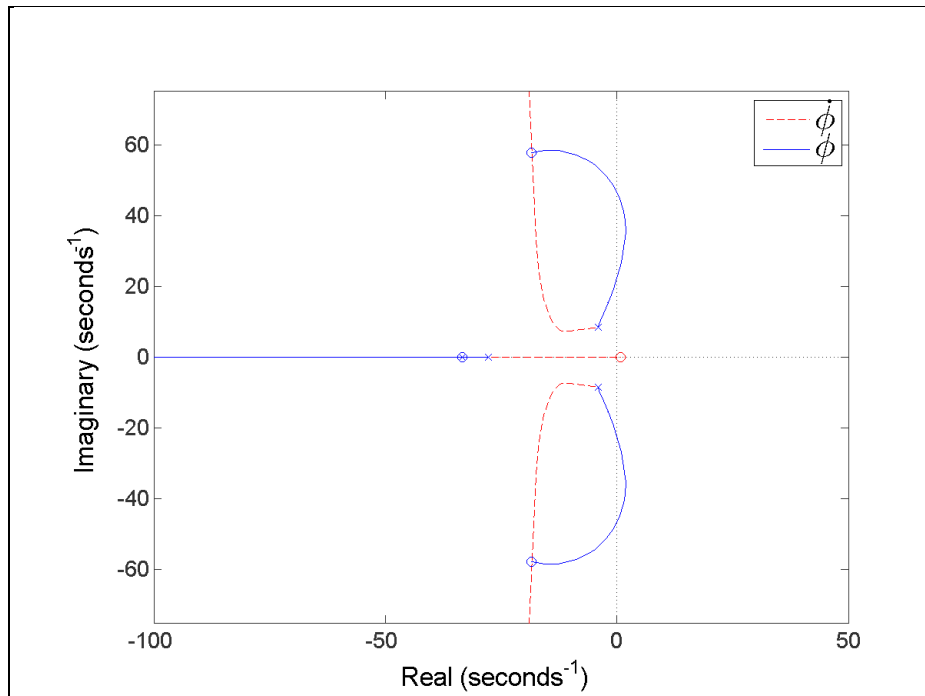


Figure 5. Root locus.

The Bode plot in figure 6 shows the controlled response decline beyond 2 Hz for roll and at about 8 Hz for roll rate. Roll features a gain margin of about 4.6 dB and phase margin of about 42°. The Bode plot illustrates that the controlled roll rate characteristics are excellent; -180° in phase is never crossed and the phase margin is about 40°.

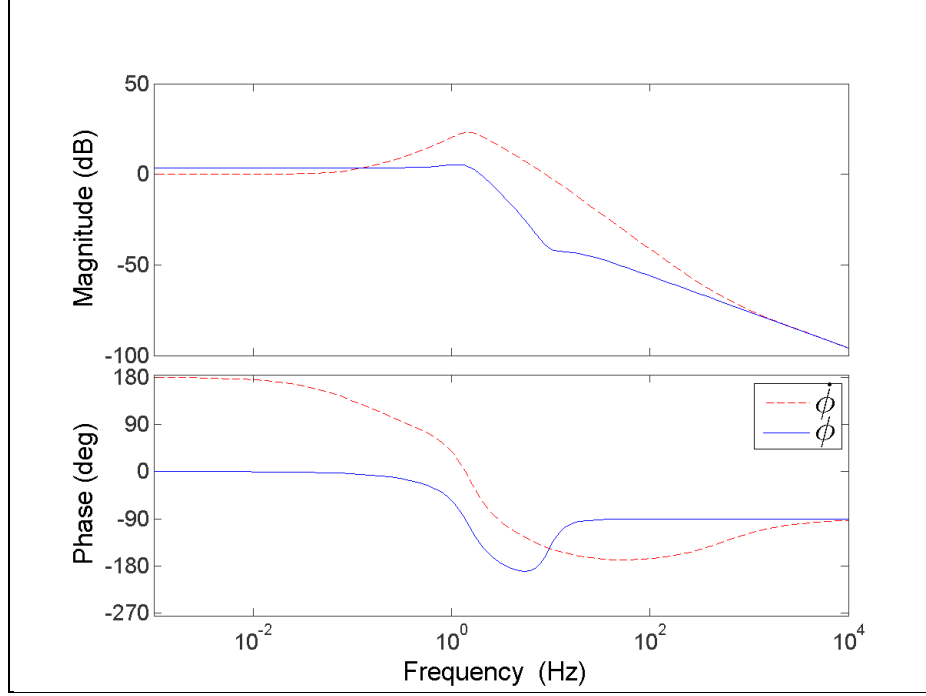


Figure 6. Bode diagram.

5. Simulation Setup

The nonlinear dynamics were implemented in a simulation environment to assess full-spectrum system performance. A fourth-order Runge-Kutta scheme was used to integrate the equations of motion. System properties are provided in table 1. The Mach number of interest was 0.49. The axial moment of inertia was obtained by solid modeling and measurement. Semi-empirical aeroprediction in the PRODAS (34) Finner code and parameter identification using Bayesian filter error methods from wind tunnel data were applied to estimate the aerodynamic coefficients. Actuator time constant and delays came from benchtop laboratory and wind tunnel data. System properties in table 1 were also used for the stability analysis.

Monte Carlo simulations were performed. System properties were varied in each Monte Carlo replication according to the uncertainties given in table 2. Bias and random errors were also added to the canard deflections, roll feedback, and roll rate feedback.

Table 1. System properties.

Property	Value	Unit
M	0.49	—
D	0.08	m
I_{XX}	0.0044	kg-m ²
C_{lp}	-6.76	—
CP^R	0.82	cal.
$C_{N\alpha}^C$	0.674	—
C_l	0.0263	—
τ	0.015	s
t_D	0.030	s
K_ϕ	0.0225	—
$K_{\dot{\phi}}$	0.0021	—

Table 2. System uncertainties (1 standard deviation).

Property	Value	Unit
D	0.1	%
I_{XX}	10	%
C_{lp}	30	%
CP^R	15	%
$C_{N\alpha}^C$	30	%
C_l	30	%
τ	20	%
t_D	20	%
δ_B	1	deg
ϕ_B	1	deg
ϕ_R	1	deg
$\dot{\phi}_B$	0.1	Hz
$\dot{\phi}_R$	0.1	Hz

6. Experimental Setup

6.1 Airframe, Instrumentation, and Wind Tunnel Facility

Experiments were conducted on the low-cost, gun-hard maneuver control system in a wind tunnel. Figure 7 shows an airframe that featured a hemispherical nose, increasing body diameter with length toward the base (to 80 mm maximum), and six fins. Détentes in the fins allowed cant angles of 0° and 2° to examine the effect of static roll torque. The majority of the maneuver system was internally mounted in the ogive of the airframe. The DSP, batteries, and S-band

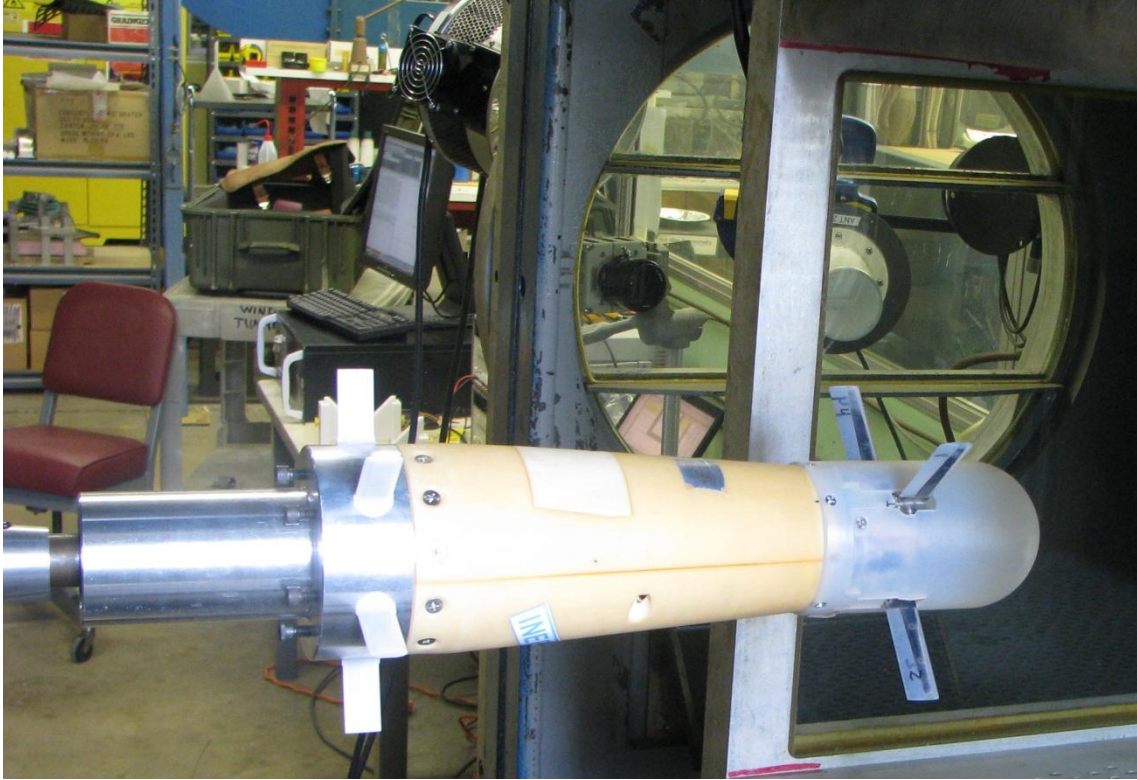


Figure 7. Model mounted in wind tunnel with high-speed camera and telemetry data acquisition.

transmitter and antenna were contained in the midbody of the airframe. The airframe was mounted to a sting in the wind tunnel and free to rotate about the longitudinal axis through a bearing.

In this experimental setup, bearing friction, which is not present in free flight, adds another moment to the roll dynamics. The experimental model was spun in the lab to estimate the moment due to bearing friction. A simple linear model of the form $L_{\mu} = \text{sgn}(\phi) F_{\mu}$ was used to obtain an experimentally derived value of -0.0604 Nm for the bearing friction moment.

An optical encoder with 8192 counts per revolution mounted in the base of the airframe measured the roll angle of the body with respect to the sting (wind tunnel). This measurement was differentiated on the DSP to estimate roll rate.

A telemetry ground station acquired the data transmitted from the wind tunnel model. High-speed photography recorded the motion of the airframe in the wind tunnel. The telemetry ground station and helical antenna and high-speed camera are evident in the background of figure 7.

The wind tunnel was located at the Edgewood Area of Aberdeen Proving Ground, MD. This tunnel features a 20- × 20-in cross section and can accommodate Mach numbers from about 0.5 to 1.2. A Mach of 0.48–0.49 was used for experiments. Figure 8 shows a typical velocity profile as the tunnel ramps up to steady state Mach number.

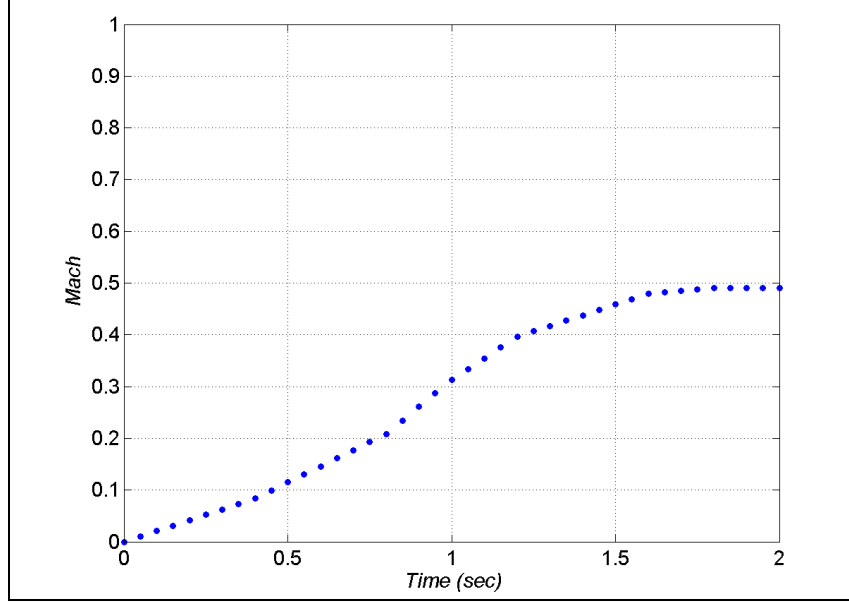


Figure 8. Representative wind tunnel profile.

6.2 Procedure

The roll control commenced during experiments based on the airframe reaching a roll rate threshold. The roll rate threshold was achieved either by deflecting canards or canting fins and starting the wind tunnel. For a given experiment, the roll rate threshold value and initial canard deflection were programmed into the DSP through a laptop with the model sitting on a bench. The model was then mounted in the wind tunnel, and the batteries were connected. As the wind tunnel blow began, the model spun to the roll rate threshold and then performed controlled deflections; telemetry and high-speed camera data were recorded. After the wind tunnel blow ended, the model was removed from the tunnel, power was turned off, data was reviewed, and the cycle repeated for the next experiment.

7. Results

7.1 Nonlinear Simulation

Simulations were performed according to the setup described earlier. Some nominal responses for an initial roll rate of 10 Hz, zero angle of attack, and no fin cant are shown in figures 9–11. The projectile body completes one revolution prior to locking into the “X” configuration at $\phi = 405^\circ$ (alternately, $360N + [45 \ 135 \ 225 \ 315]$ degree roll could have been the symmetry point) with a steady-state roll error of $<1^\circ$. Roll rate decreases to zero by about 0.3 s. Some overshoot and oscillation is apparent in the roll and roll rate, but using the flight and actuation model in the control algorithm provides sufficient performance for a nominal simulation.

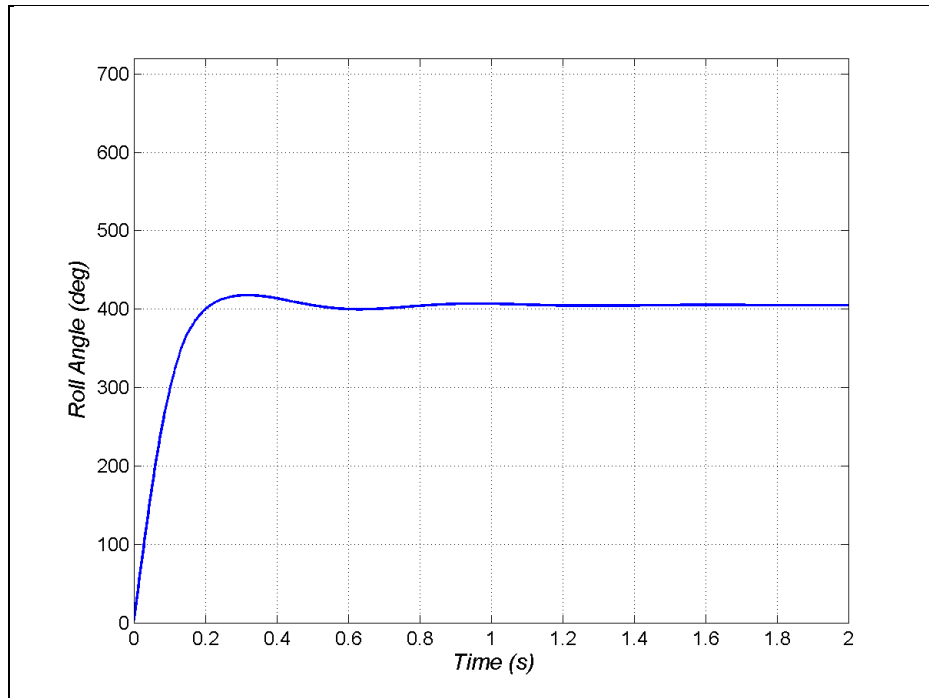


Figure 9. Nominal controlled response without fin cant at zero angle of attack and 10-Hz initial roll rate – roll angle.

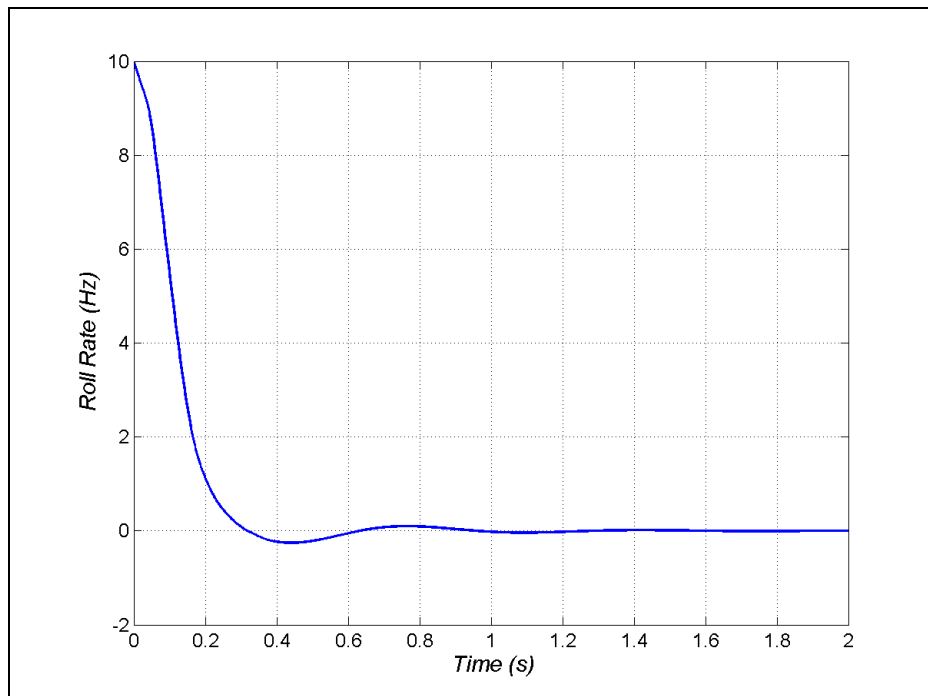


Figure 10. Nominal controlled response without fin cant at zero angle of attack and 10-Hz initial roll rate – roll rate.

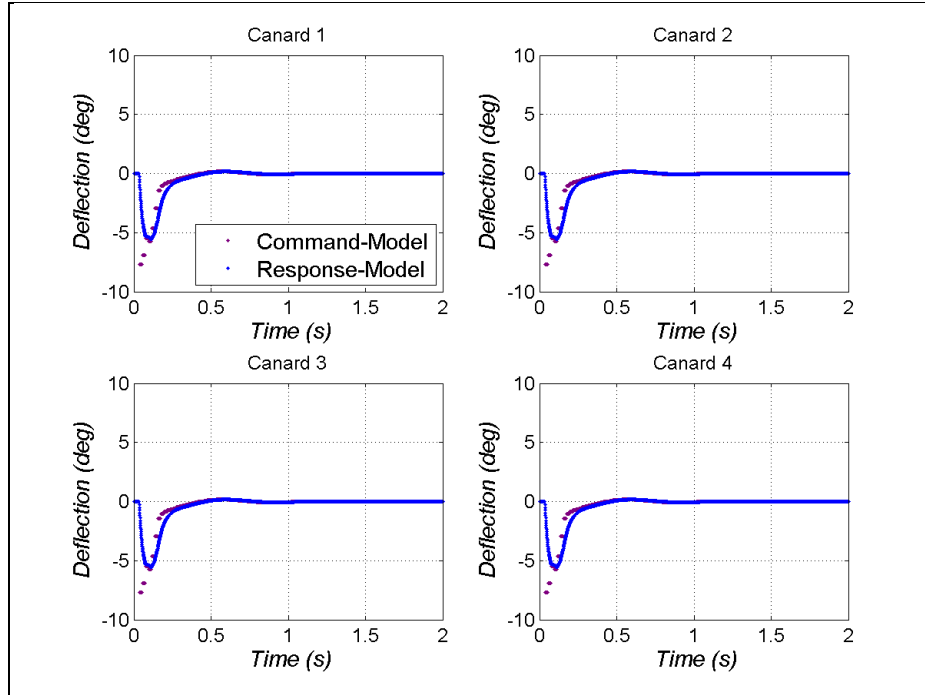


Figure 11. Nominal controlled response without fin cant at zero angle of attack and 10-Hz initial roll rate – deflections.

The deflection history for all four canards for the nominal simulation is presented in figure 11. Canards deflect in the negative direction to decrease the initially positive roll rate. The difference between the commands and modeled response is due to the delay and lag. Sample and hold at 50 Hz is also present in the data.

Monte Carlo simulation results for 500 samples at zero angle of attack are provided in the next six figures. For these simulations, initial roll was randomized between 0° and 360° according to a uniform random number generator, and initial roll rate was randomly drawn from a normal distribution with a standard deviation of 10 Hz. All other parameters were randomized with a normal distribution, with mean and standard deviation provided in tables 1 and 2. Each canard featured unique values for lag, delay, and bias.

Histograms of the roll angle manipulated by a modulo at 2 s are given in figure 12. Roll symmetry points of 45° , 135° , 225° , and 315° are dashed red vertical lines. Many simulations are grouped around the 45° and 225° symmetry points with a few distributed about the 135° and 315° roll locations. The reason behind these groupings is likely the interaction of the initial roll rate and the roll control effectiveness, as seen for the nominal simulation responses. Essentially, the roll rate is controlled at a time where 45° or 225° is the closest roll symmetry location.

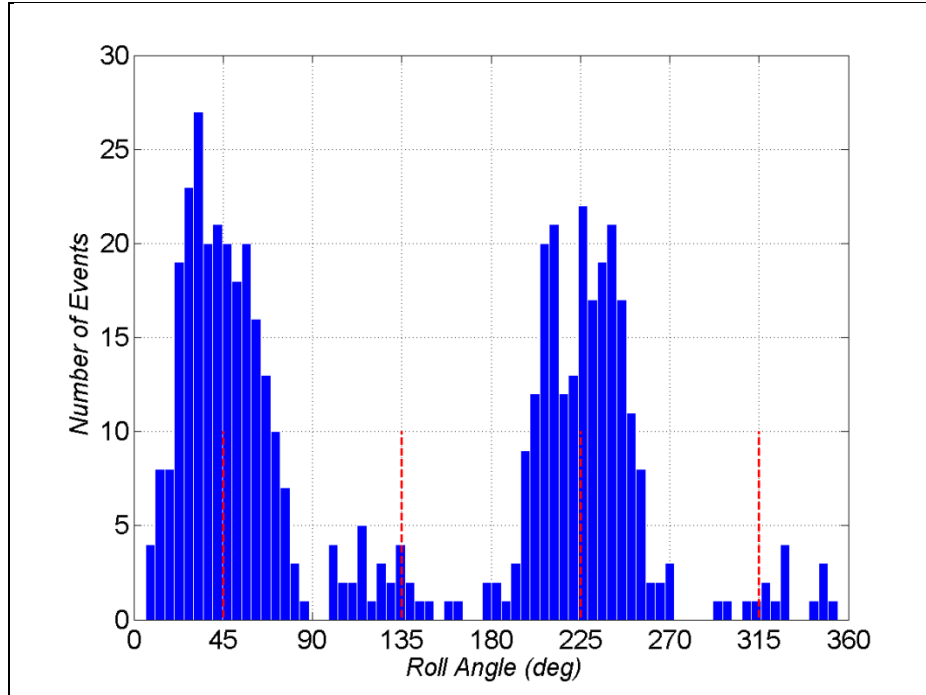


Figure 12. Monte Carlo controlled response without fin cant at zero angle of attack and 10-Hz initial roll rate – modulo roll angle histogram at 2 s.

Individual Monte Carlo samples for the roll rate and deflections are shown in figures 13 and 14. The dashed red lines represent plus and minus one standard deviation about the mean of all simulations. The initial roll rate is reduced to <1 Hz by about 0.3 s. The deflections show a region close to zero time with small deflection due to the delay and lag, followed by a moderate deflection (standard deviation of about 5°) for a few hundred milliseconds, then a near-constant value as the desired control is achieved. Bias errors in the roll rate and deflections are illustrated in these results.

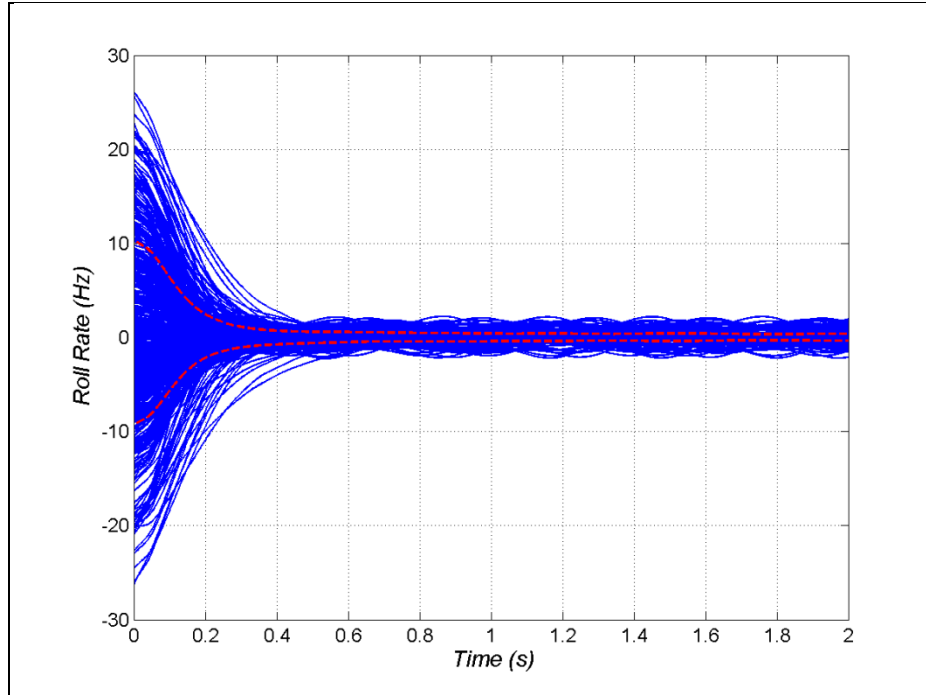


Figure 13. Monte Carlo controlled response without fin cant at zero angle of attack and 10-Hz initial roll rate – roll rate.

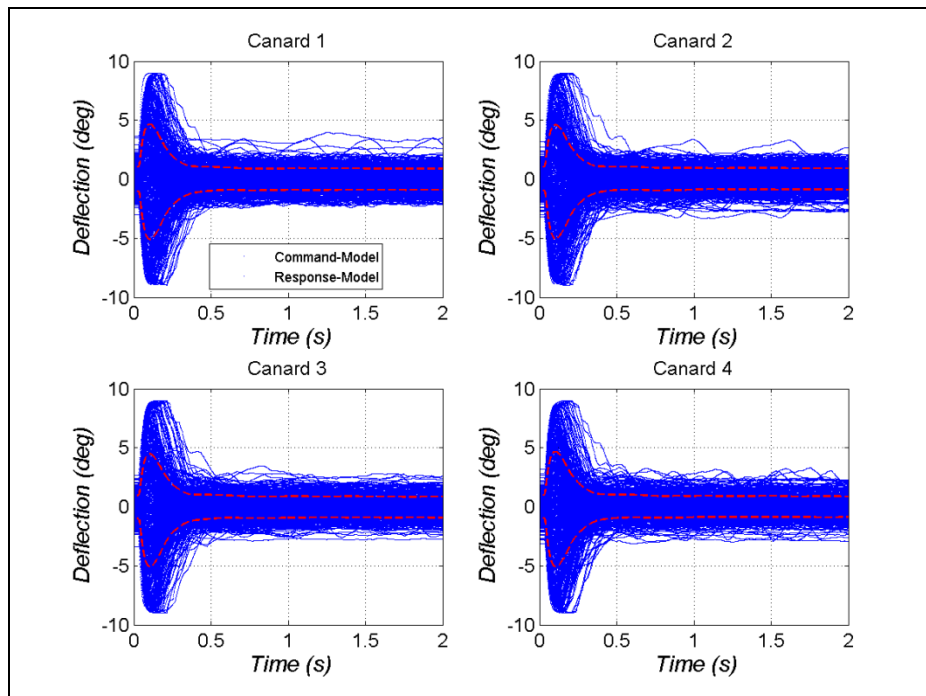


Figure 14. Monte Carlo controlled response without fin cant at zero angle of attack and 10 Hz initial roll rate – deflections.

Monte Carlo analysis was conducted for zero angle of attack with fin cant. These results, given in figures 15–17, are similar to the no fin cant case. The roll histograms are grouped at 45° and 225° . The roll rate falls below 1 Hz statistically within about 0.3 s. Deflections peak within the first few hundred milliseconds and feature an offset on average of about -1° to counteract the fin roll torque. A feedforward gain resulting in a deflection command of -0.9° was used in these simulations. Results did not change appreciably without the feedforward gain.

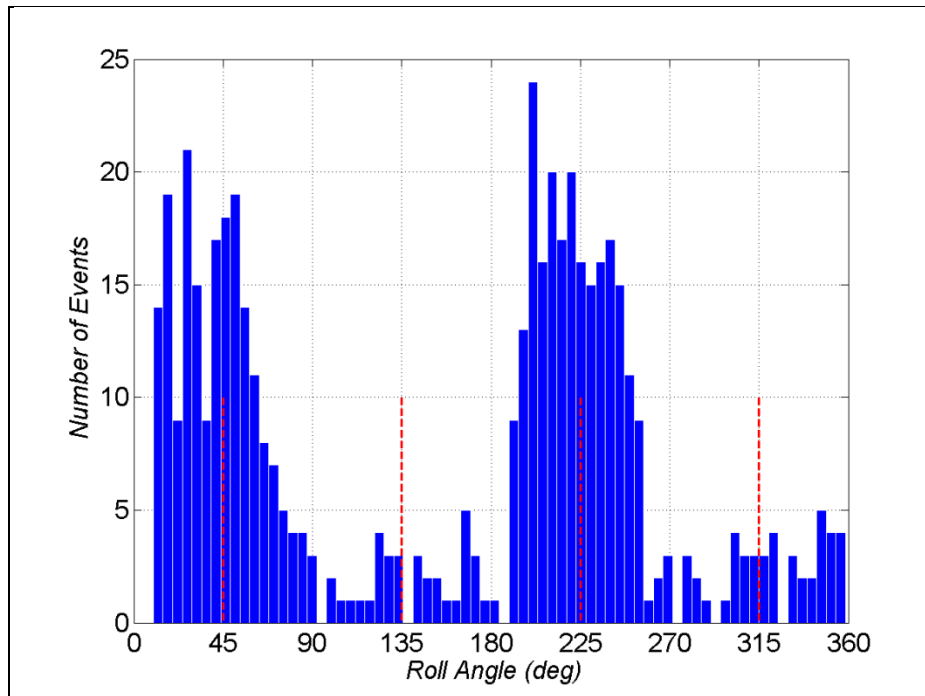


Figure 15. Monte Carlo controlled response with 2° fin cant at zero angle of attack and 10-Hz initial roll rate – modulo roll angle histogram at 2 s.

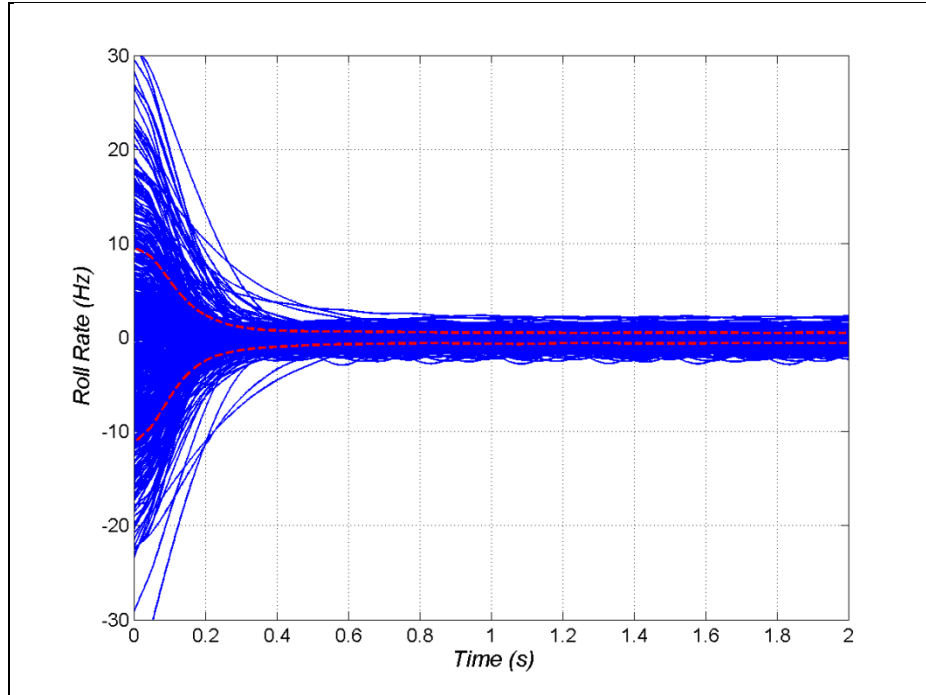


Figure 16. Monte Carlo controlled response with 2° fin cant at zero angle of attack and 10-Hz initial roll rate – roll rate.

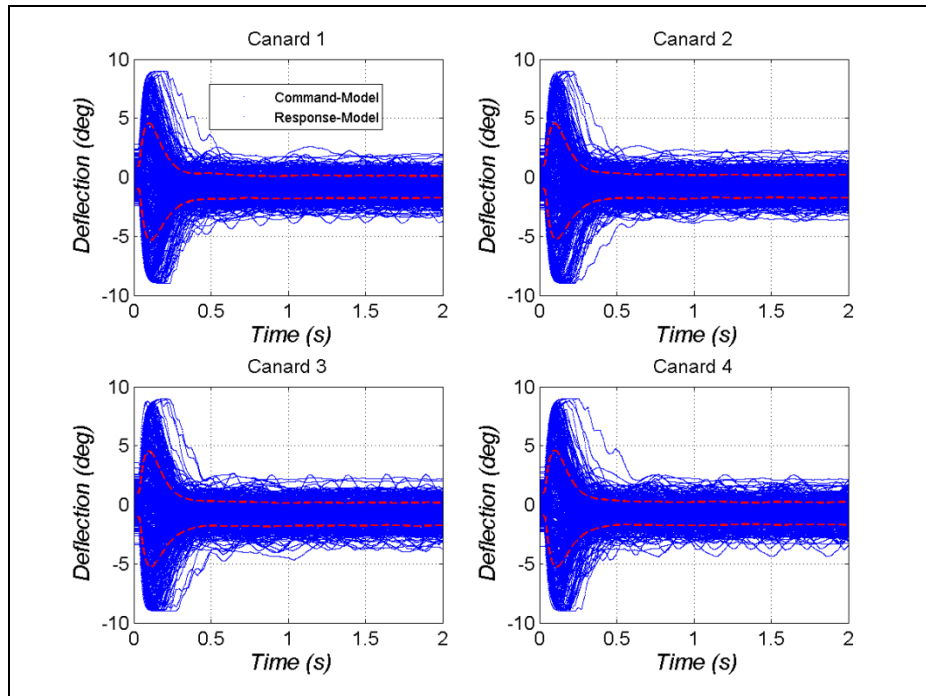


Figure 17. Monte Carlo controlled response with 2° fin cant at zero angle of attack and 10-Hz initial roll rate – deflections.

7.2 Experiment

Wind tunnel experiments were performed according to the setup and procedure outlined previously. Scatter in the experimental data is due to bit errors in the telemetry. Initial experiments were designed to assess the open-loop performance of the maneuver system in the wind tunnel. Maneuver system properties (e.g., bias, linearity), aerodynamic estimates, flow conditioning, and accuracy of model fixturing in the tunnel were investigated during these initial experiments.

One series of experiments to address these phenomena swept each canard through a sequence of angles every 800 ms. This method is illustrated by examining figures 18 and 19 in tandem. As the tunnel started, canard 1 was deflected to 4° . Once roll rate exceeded 2 Hz, canard 1 changed value to 0° , -4° , 4° , -8° , 8° with all other canards held to zero. After canard 1 finished sweeping through these commands, canard 2 began an equivalent sweep. This process was repeated until all canards were cycled. The wind stopped just as canard 4 began deflections so these data were not captured. Bias in the roll rate is apparent in these results; -4° and -8° deflections yield about a -2 and -4 Hz roll rate, respectively, while 4° and 8° deflections produce 2.5 and almost 5 Hz roll rate, respectively. With just the wind tunnel data, it is indeterminate whether this is due to some mix of maneuver system bias or nonlinearity or some cross-flow due to flow conditioning or model fixturing. Unsteady flow effects are also present. Regardless, these measurements provide experimental evidence of nonideal response that the maneuver control system must sufficiently address.

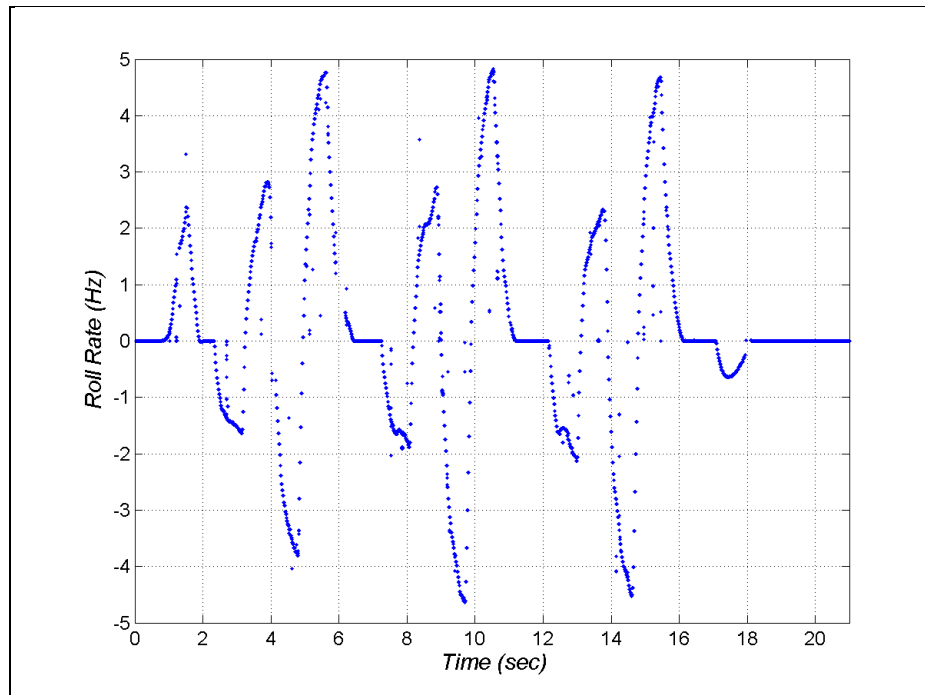


Figure 18. Individual canard impulse response without fin cant at zero angle of attack – roll rate.

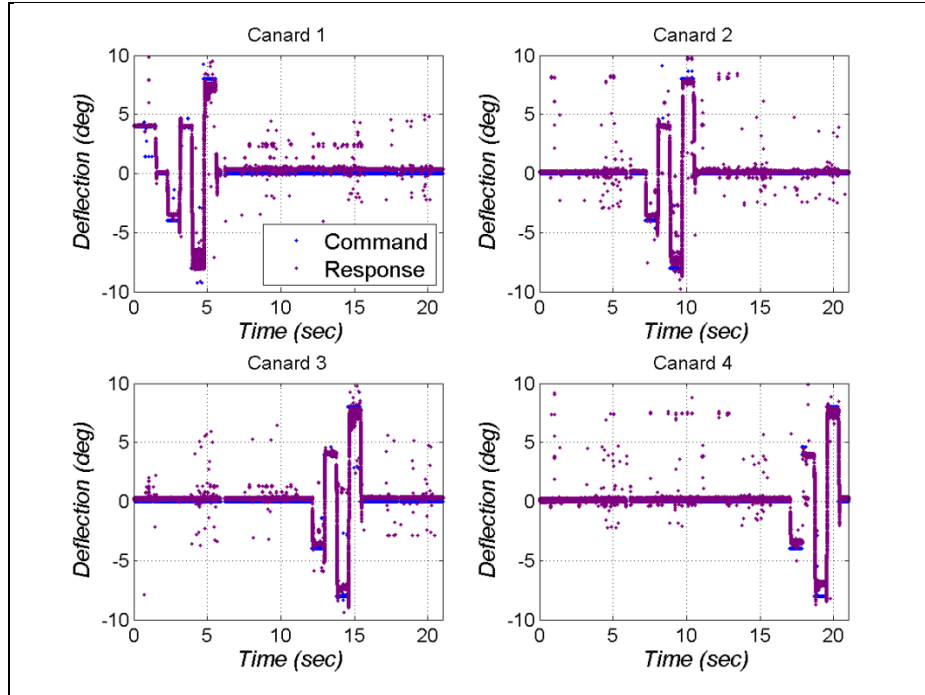


Figure 19. Individual canard impulse response without fin cant at zero angle of attack – deflections.

Another set of experiments was designed to determine maneuver system response in the tunnel at 0° angle of attack with 2° fin cant and collective deflection. These data are provided in figures 20 and 21. Fins were used to increase the roll rate as the wind commenced. Once the 1-Hz roll rate was reached, all canards deflected to 0° , -0.5° , -1° , -1.5° , and -2° at 800-ms intervals. Deflecting all canards to -0.5° decreased the roll rate. As the deflection angle changes to -1° , the canard and fin roll torques are nearly equal and opposite. Friction in the roll bearing becomes more important as the roll rate approaches zero. The precise characterization of bearing friction is likely highly nonlinear near zero rotation speed and was not undertaken. Bearing friction is not acting during free-flight, and this phenomenon adds difficulty to the problem of controlling roll in the wind tunnel, as at very low rotational speeds, overcoming the bearing friction becomes more important. Increasing the deflection to -1.5° yields a negative roll rate, and -2° deflection increases the negative roll rate. As another cycle of deflections began, however, the wind stopped at about 6–7 s. This experiment provides a value for canard deflection necessary to overcome the bearing friction at zero roll rate and also the deflection that may be used in a feedforward gain construction during control with fin cant.

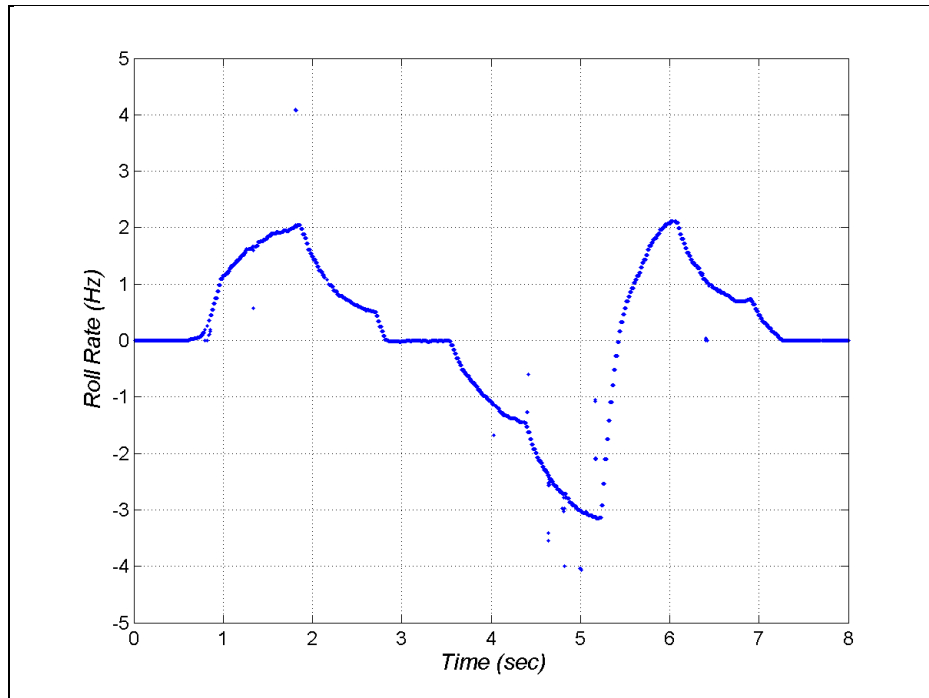


Figure 20. Group canard impulse response with 2° fin cant at zero angle of attack – roll rate.

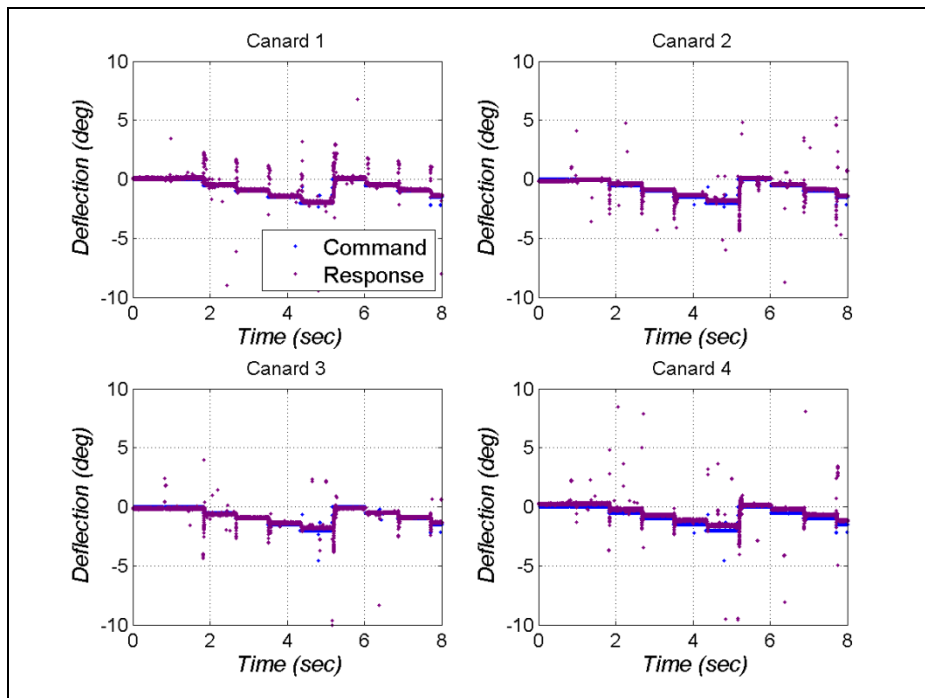


Figure 21. Group canard impulse response with 2° fin cant at zero angle of attack – deflections.

Control was performed in the wind tunnel. These data provided experimental support for the performance of the maneuver control system and an opportunity to validate the modeling and simulation. Figures 22 and 23 provide the experimental data for zero angle of attack and no fin cant and the corresponding Monte Carlo analysis. Here, the canards were initially deflected to 4° , and control began once the wind started and the roll rate exceeded 10 Hz. In the experiment, the roll was controlled within about 0.3 s, similar to previous simulations. Roll rate and deflection response lie within the 1 standard deviation bounds of the Monte Carlo simulations for the majority of the time. Differences in the roll behavior (and subsequent deflection commands using roll and roll rate feedback) that occur as the roll rate passes through zero are likely due to nonlinear bearing friction or unsteady, nonlinear aerodynamics. Excellent agreement between experiment and simulation will only improve further as aerodynamic and maneuver system characterizations mature.

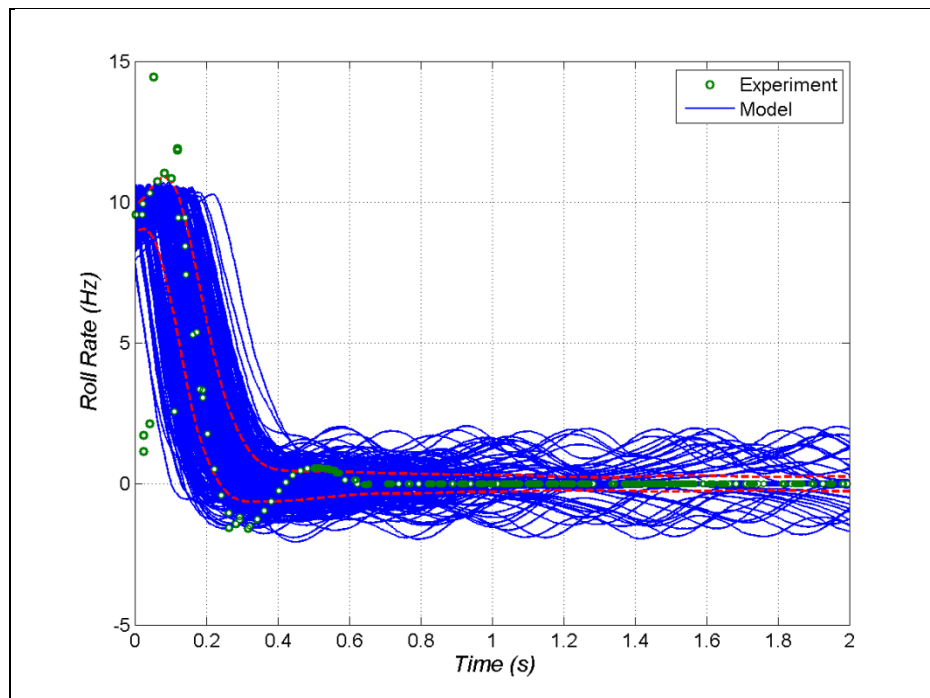


Figure 22. Monte Carlo simulation and experimental controlled response without fin cant at zero angle of attack at 10 Hz initial roll rate – roll rate.

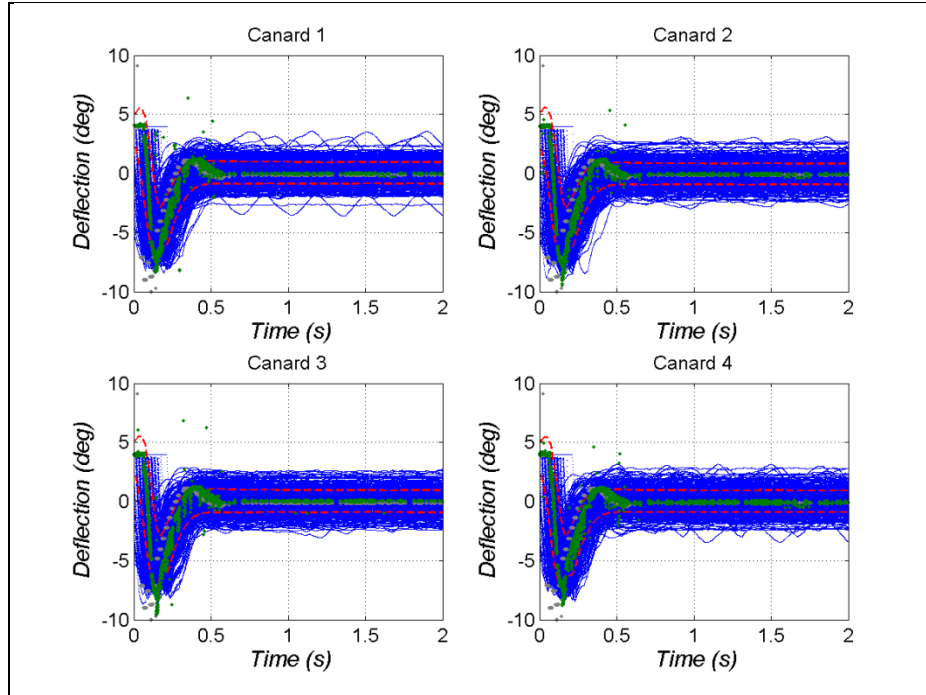


Figure 23. Monte Carlo simulation and experimental controlled response without fin cant at zero angle of attack at 10 Hz initial roll rate – deflections.

Experiments were repeated at the same conditions (zero angle of attack, no fin cant, 10-Hz initial roll rate). These results are presented in figures 24–26. The roll angle increased prior to locking into the nearest symmetry point (1305°) with about a 37° error. Roll rate decreased with some oscillation near zero. The concomitant deflections show that the demand after the roll rate is zero is almost 1° because of the roll angle error; however, the static bearing friction is too high to roll the model in the wind tunnel. This response agrees with the collective deflection open-loop experiments, where a deflection of 1.5° was required to break the bearing friction from rest. This phenomenon is not present in free-flight.

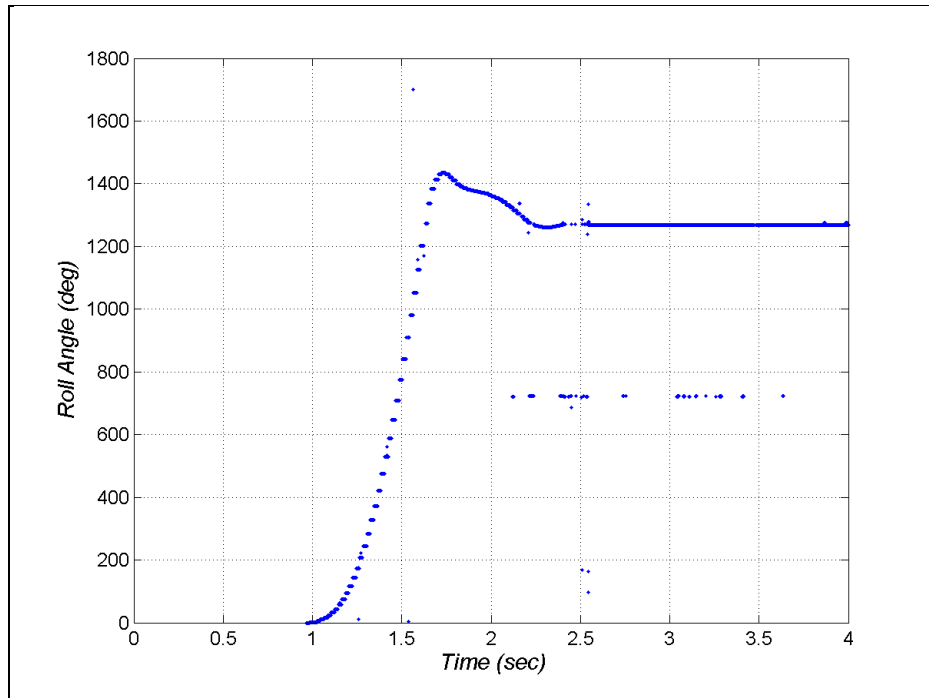


Figure 24. Controlled response without fin cant at zero angle of attack at 10-Hz initial roll rate – roll angle.

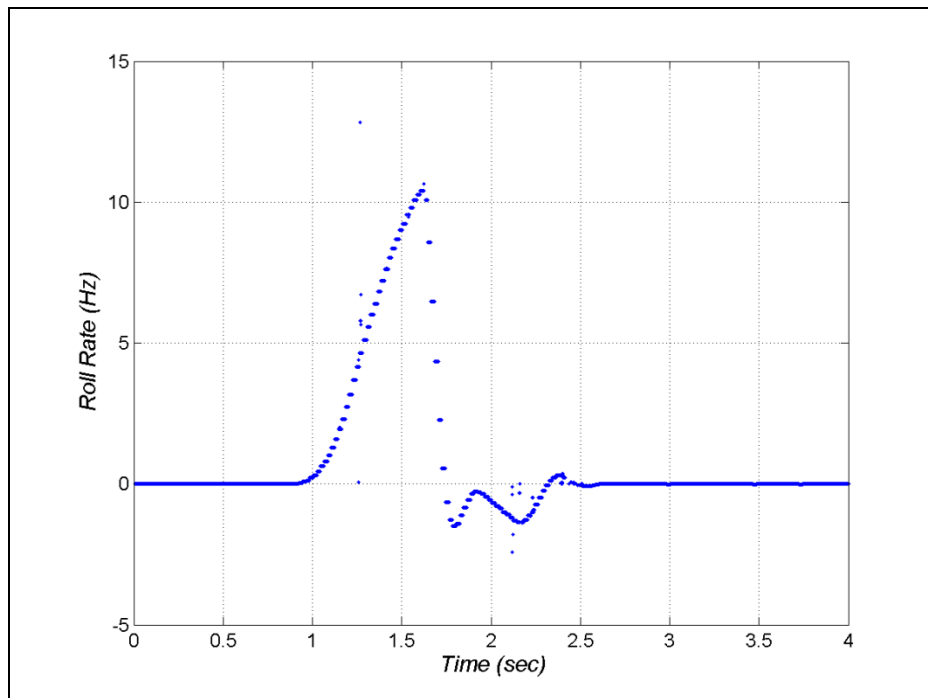


Figure 25. Controlled response without fin cant at zero angle of attack at 10-Hz initial roll rate – roll rate.

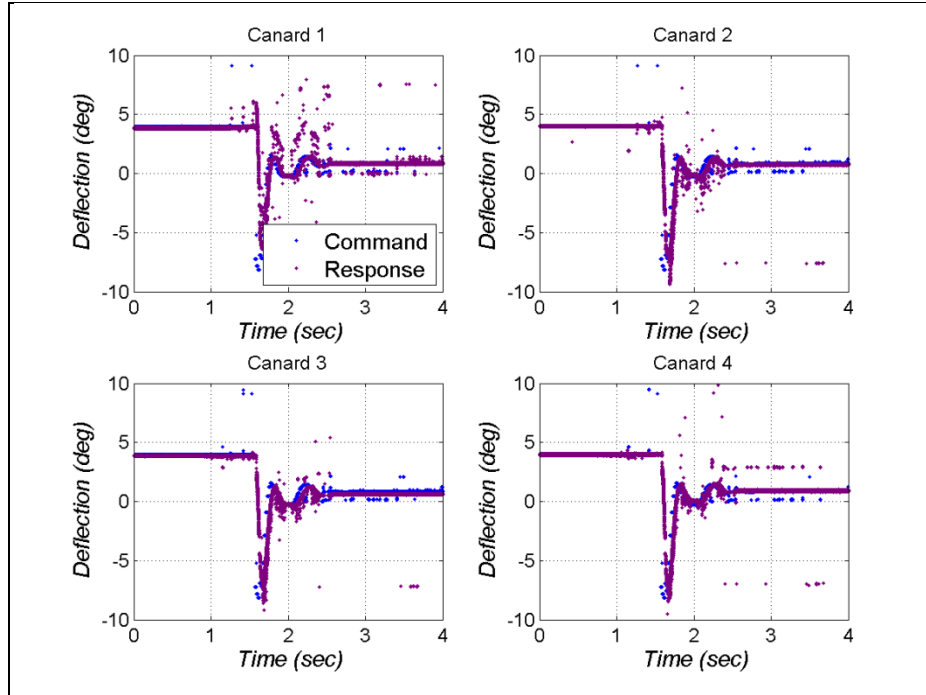


Figure 26. Controlled response without fin cant at zero angle of attack at 10-Hz initial roll rate – deflections.

Fin cant of 2° was emplaced on the model, and controlled experiments were executed. For the results in figures 27–29, a feedforward gain yielding a deflection of -0.8° was used to combat the static roll torque of the fins. Experimental roll was within 1° of the desired point (1125°), and roll rate was within 1 Hz of zero within about 200 ms from start of control. The -0.8° deflection offset for longer times was to counteract the fin cant. The long (>2 s) drop-out in data was due to the transmitting telemetry antenna facing away from the receiving antenna once roll control started.

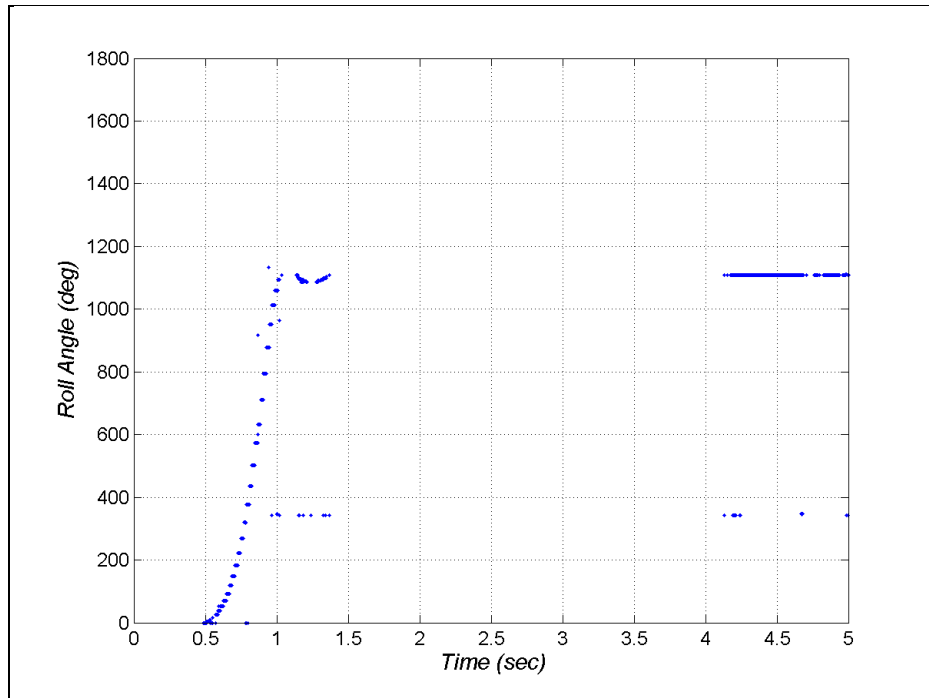


Figure 27. Controlled response with 2° fin cant at zero angle of attack at 10-Hz initial roll rate – roll angle.

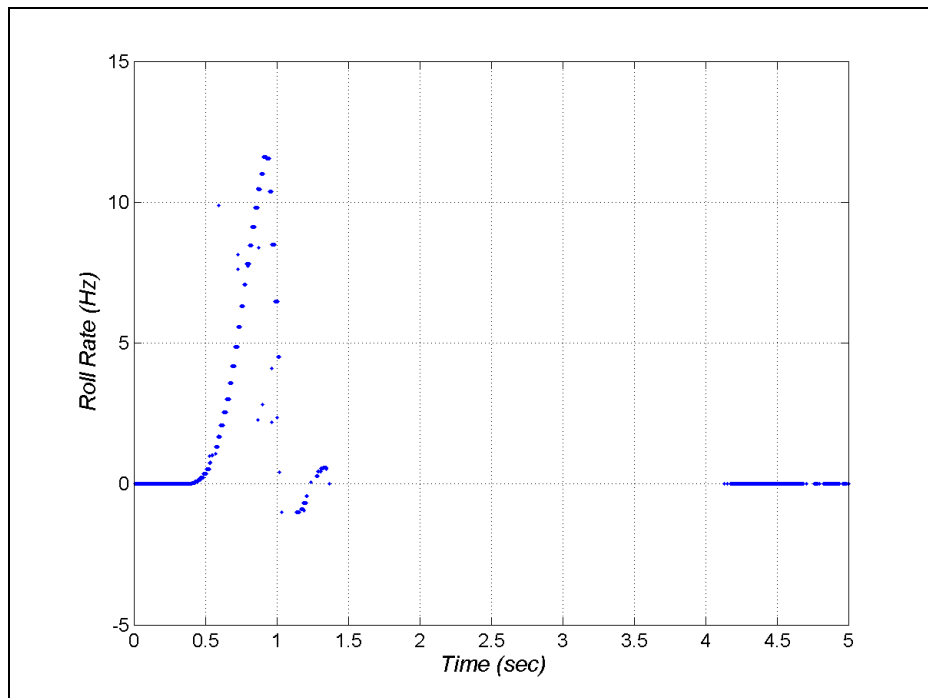


Figure 28. Controlled response with 2° fin cant at zero angle of attack at 10-Hz initial roll rate – roll rate.

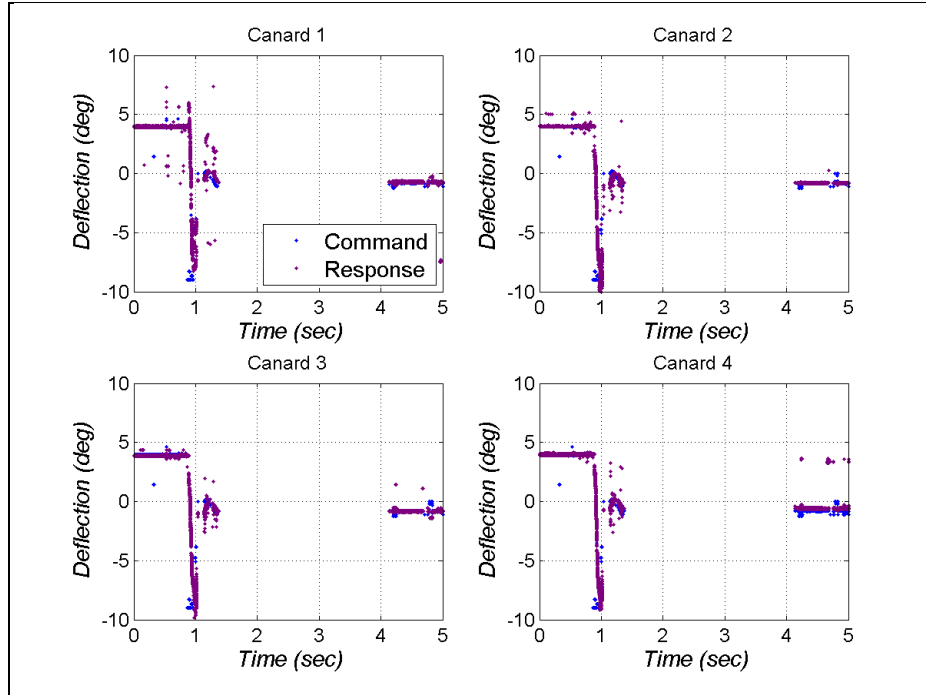


Figure 29. Controlled response with 2° fin cant at zero angle of attack at 10-Hz initial roll rate – deflections.

The effect of initial roll rates was studied by keeping the angle of attack at 0°, fin cant to 2°, and setting the threshold for control to start at 2 Hz. The roll, roll rate, and deflections for this case are shown in figures 30–32. As expected, the response was improved for lower initial roll rate. Again, the feedforward gain was used, and the roll was $<2^\circ$ from the symmetry point (225°) by the end of the blow. Some slow transient in roll response was evident; there was about 15° of error when roll rate was regulated to zero. Deflection histories illustrate that less control demand is required to sufficiently control the model when initial conditions are closer to the desired states.

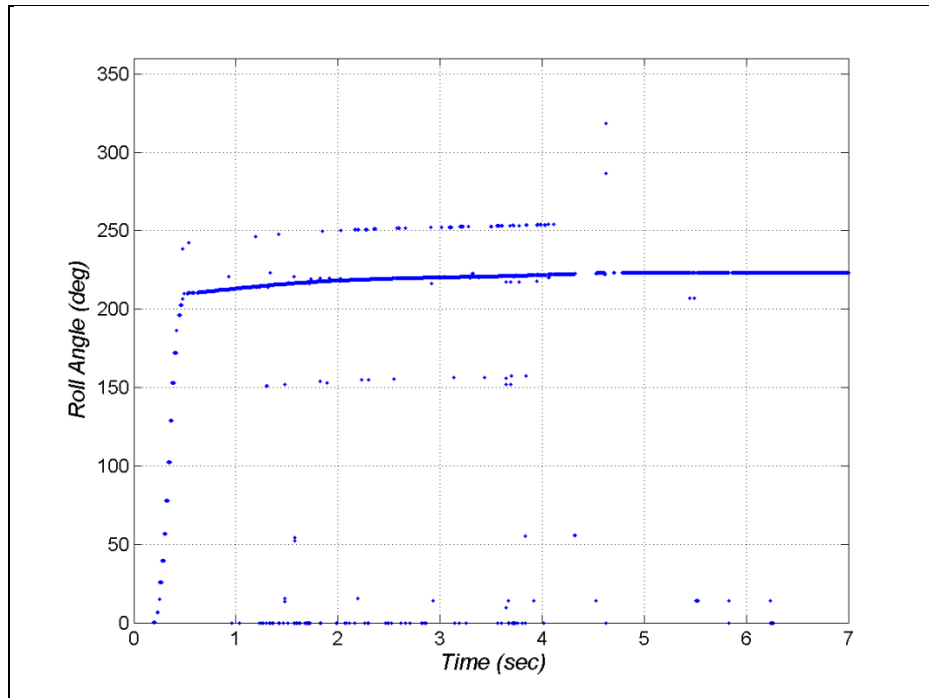


Figure 30. Controlled response with 2° fin cant at zero angle of attack at 2-Hz initial roll rate – roll angle.

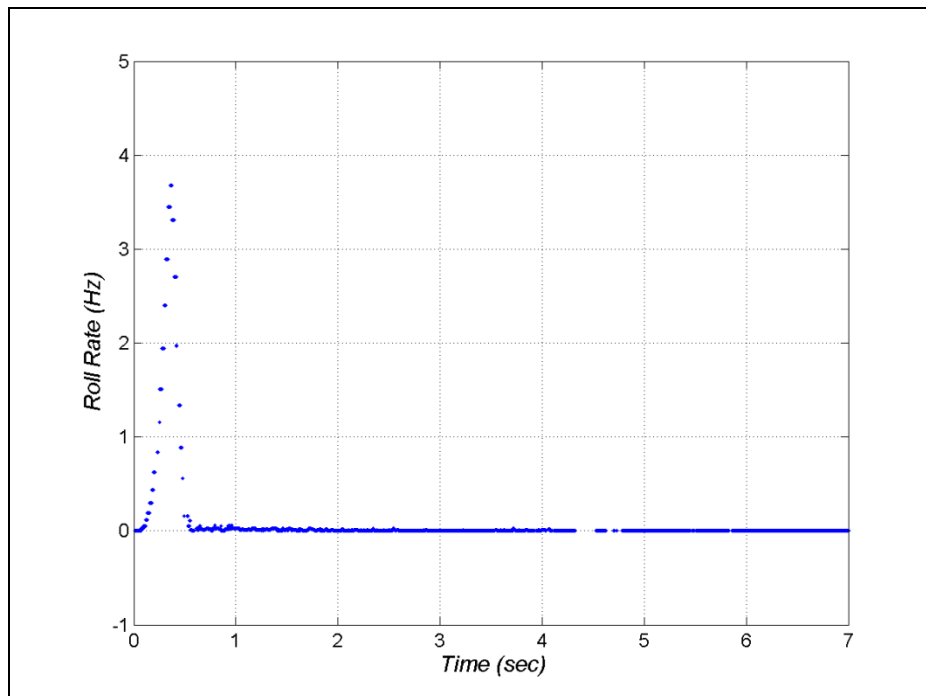


Figure 31. Controlled response with 2° fin cant at zero angle of attack at 2-Hz initial roll rate – roll rate.

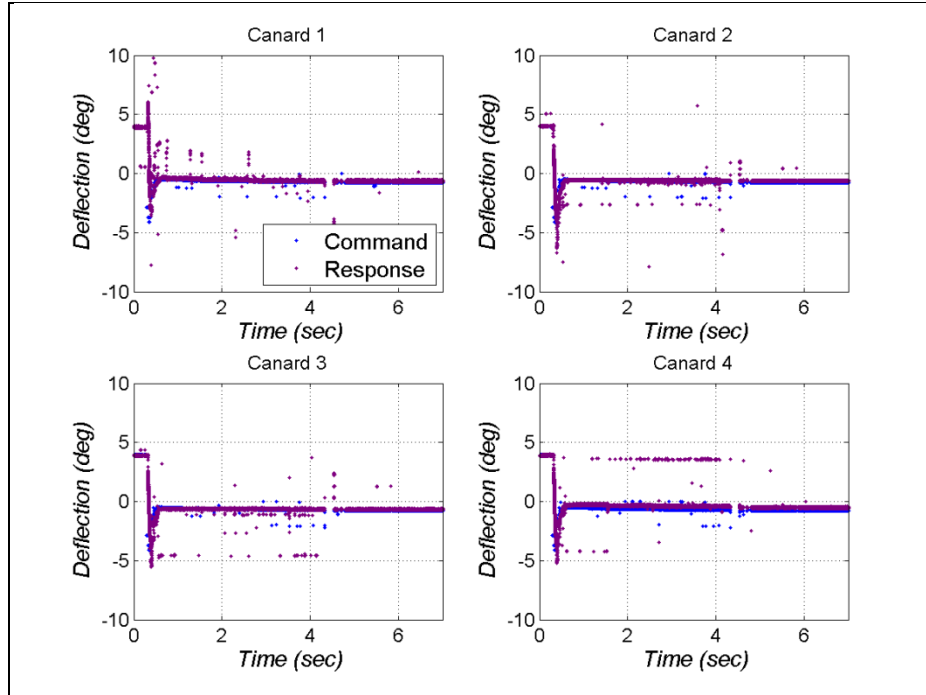


Figure 32. Controlled response with 2° fin cant at zero angle of attack at 2-Hz initial roll rate – deflections.

It is well known that the aero-mechanics of projectiles, especially while spinning, can be highly nonlinear with angle of attack. Wind tunnel experiments were conducted to assess the performance of this maneuver control system at angle of attack. The data in figures 33–35 were taken with the model at a 5° angle of attack and no fin cant. Roll is regulated to within 31° of the desired angle (1125°). Roll rate response and deflection histories are similar to previous experimental results. The roll rate response beyond the threshold for control to start and subsequent deflection commands and roll rate overshoot were slightly more dramatic since initial deflections were 8° to account for aerodynamic roll angle-dependent lifting surface effectiveness. Deflections were almost a degree after the roll rate was controlled to zero because of remaining roll error. Again, the bearing friction near roll rate zero is likely the culprit for the steady-state roll behavior.

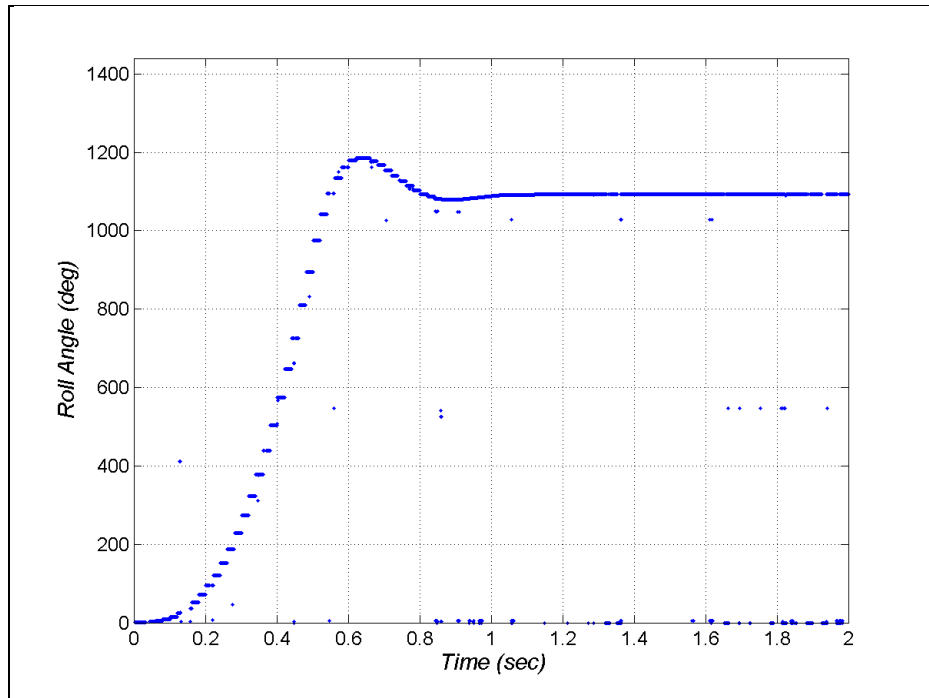


Figure 33. Controlled response without fin cant at 5° angle of attack at 10-Hz initial roll rate – roll angle.

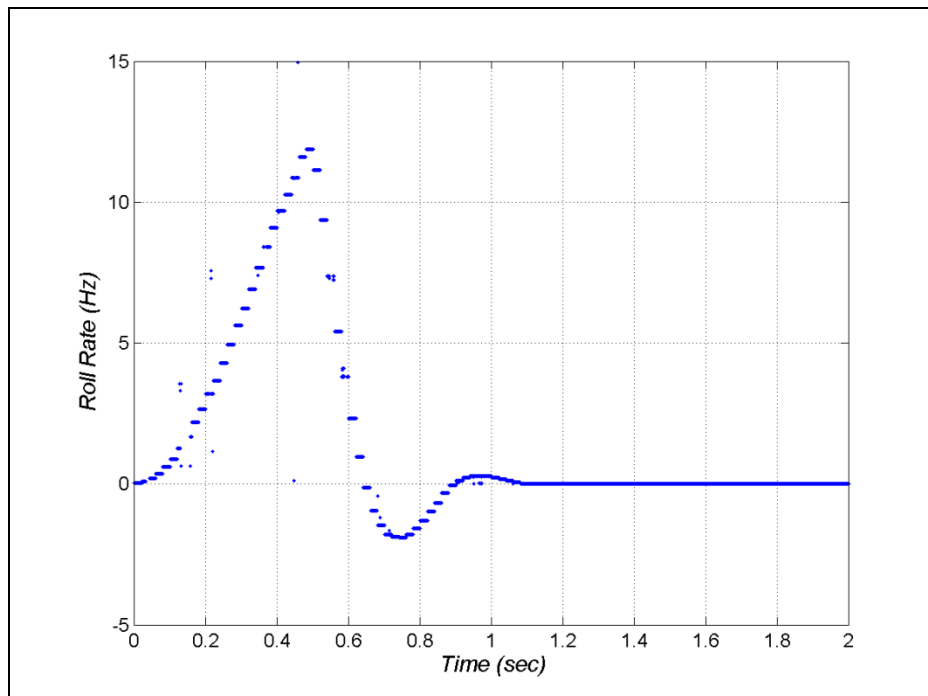


Figure 34. Controlled response without fin cant at 5° angle of attack at 10-Hz initial roll rate – roll rate.

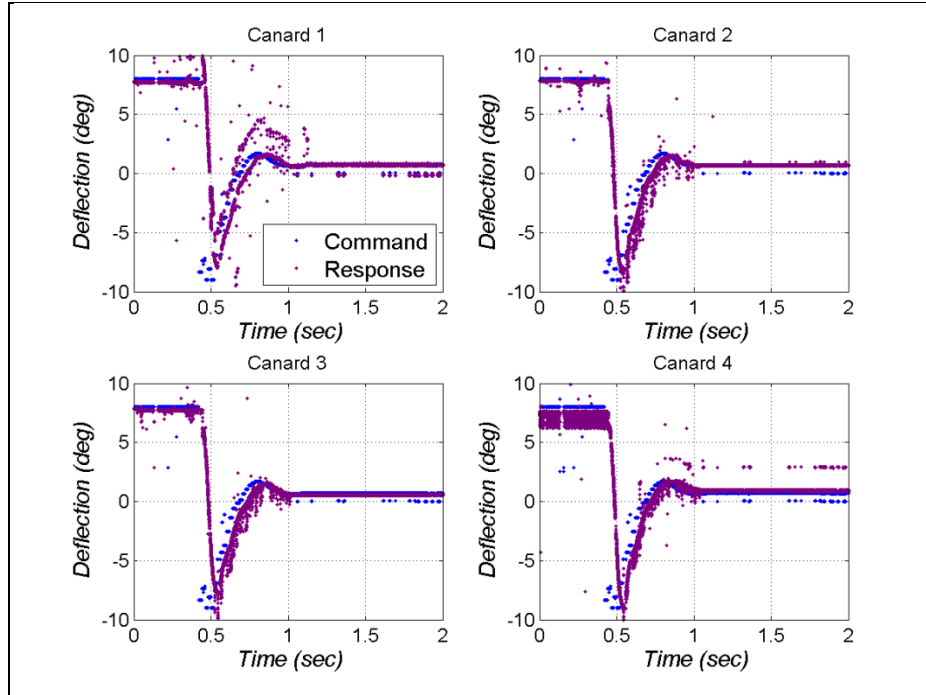


Figure 35. Controlled response without fin cant at 5° angle of attack at 10-Hz initial roll rate – deflections.

The final fundamental phenomenon under investigation was the effect of angle of attack with fin cant. These data are given in figures 36–38. The feedforward gain was not used in this experiment. Roll was regulated to about 31° of the desired angle (1305°). Roll and roll rate oscillated a few hundred milliseconds after control started, potentially because of unsteady flow interactions of canards and fins. Steady-state deflection commands exist because of the steady-state error in roll.

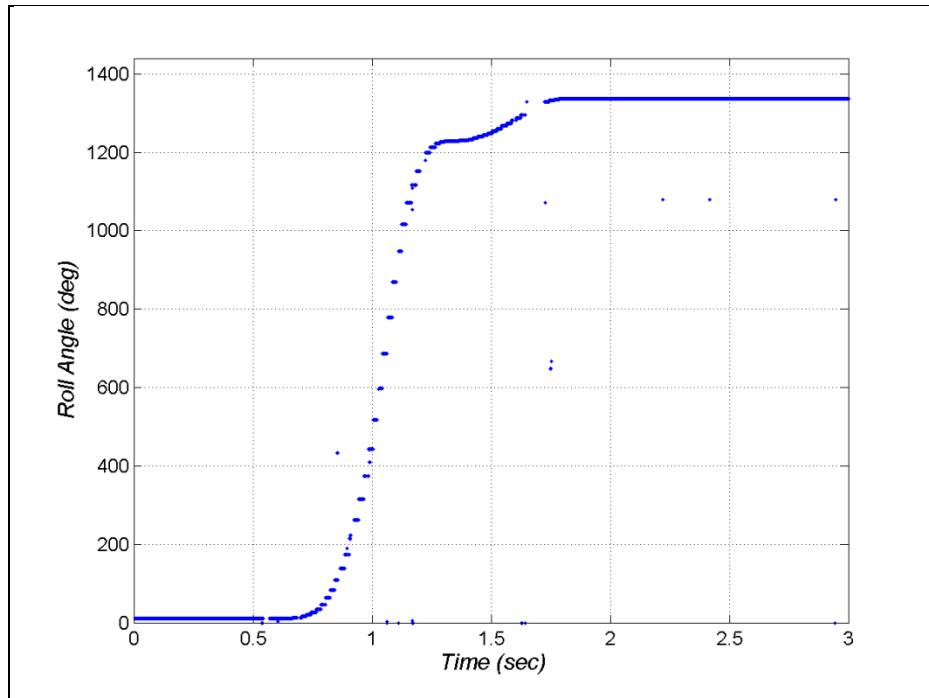


Figure 36. Controlled response with 2° fin cant at 5° angle of attack at 10-Hz initial roll rate – roll angle.

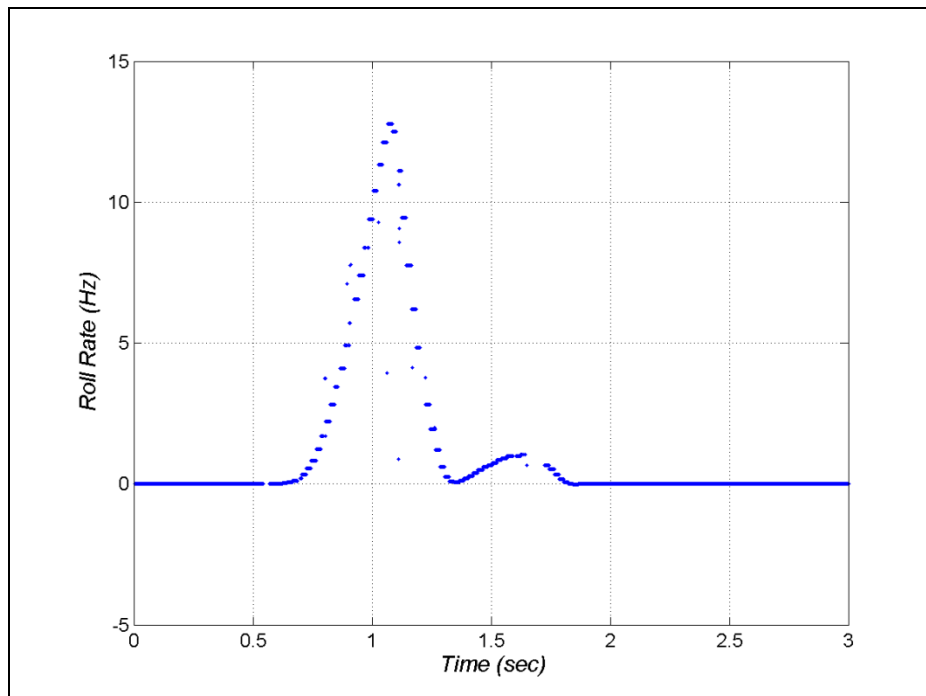


Figure 37. Controlled response with 2° fin cant at 5° angle of attack at 10-Hz initial roll rate – roll rate.

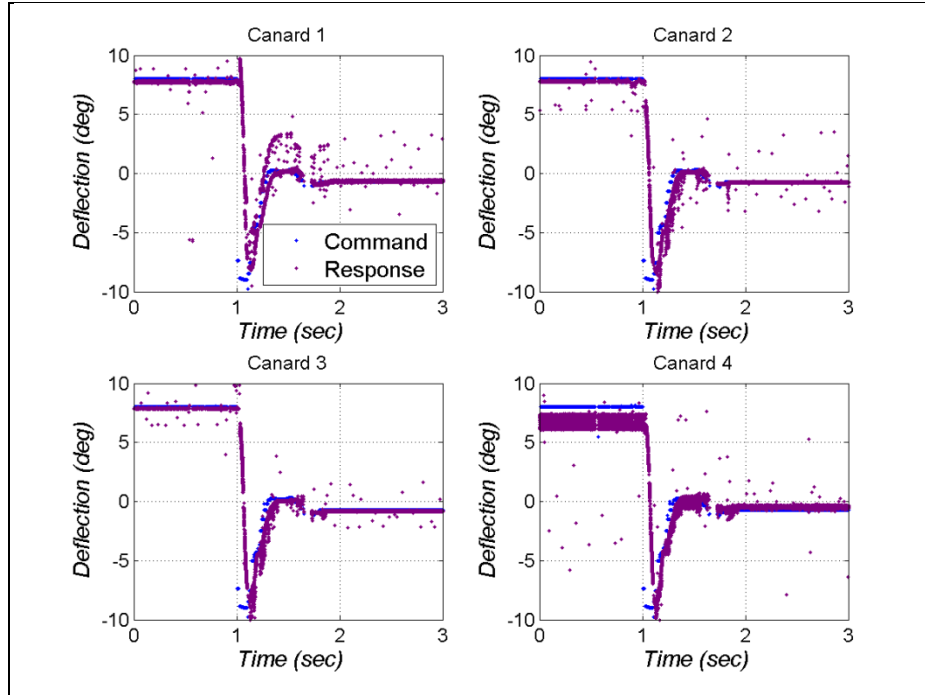


Figure 38. Controlled response with 2° fin cant at 5° angle of attack at 10-Hz initial roll rate – deflections.

8. Conclusions

The motivation for this effort is a new capability of affordable interception of targets requiring high maneuverability from gun-launched systems, which represents an enormous leap-ahead in lethal technology. The novel low-cost, gun-hard maneuver control system successfully developed and outlined in this report supports this goal. These technologies are applicable to a generic class of munitions from 60 to 155 mm in diameter. This system flies in a skid-to-turn arrangement, may feature time of flight as short as 1 s, does not have a rocket motor, and is gun hard. The approach to achieve this novel system was to use a systems approach to relax subsystem interface requirements that enabled the application of COTS devices. The approach also relied on a high-fidelity aero-mechanics characterization in the control scheme.

The mechatronics of the maneuver system was provided. The suitability of this design for survival at gun launch was assessed through laboratory shock experiments. Modeling of the actuation system was underpinned through benchtop experiments.

Dynamics of the projectile roll and actuator were derived from first principles. The aerodynamics are a major contributor to the system response; therefore, detailed modeling was undertaken. The dynamics were linearized and a formal controllability analysis illustrated that

the system was formulated properly. The linear quadratic regulator was applied for this unique system. Stability analysis evaluated closed-loop behavior and helped select optimal control gains.

Nonlinear simulations and wind tunnel experiments were described and conducted. The effects of initial roll rate, fin cant, and angle-of-attack phenomena were investigated. These results demonstrated that this maneuver control system achieves the required performance over the necessary conditions. Monte Carlo simulations showed satisfactory control within about 0.3 s over a wide range of variation in system parameters, such as mass properties, aerodynamics, actuation (delay, lag, and bias), and feedback (roll, roll rate). Wind tunnel experiments verified the modeling and simulation and further validated the low-cost, gun-hard maneuver control system. Open-loop experiments illustrated the non-ideal performance of the COTS-based maneuver system; however, the closed-loop results indicated that using appropriate dynamic modeling in the control scheme with a systems approach led to successful control. After all experimental results were reviewed, it appears that steady-state roll errors in the wind tunnel are driven by bearing friction, as cases with fin cant and zero angle of attack (i.e., when a steady, constant force other than the canards is available) feature roll error within 1° to 2° . While bearing friction in the wind tunnel rig led to reduced roll response, this phenomenon is not present in the relevant environment and Monte Carlo simulations of free-flight suggest sufficient performance.

Future efforts focus on improved aerodynamic modeling based on computational and experimental techniques. These data are essential to synthesizing the simplest, most effective controller. Pitch and yaw control are necessary for lateral maneuvers to the target. Integration with the navigation technology must be undertaken to achieve target engagements requiring high maneuverability from a gun.

9. References

1. Morrison, P. H.; Amberntson, D. S. Guidance and Control of a Cannon-Launched Guided Projectile. *Journal of Spacecraft and Rockets* **1977**, 14 (6), 328–334.
2. Grubb, N. D.; Belcher, M. W. Excalibur: New Precision Engagement Asset in the Warfight. *Fires* **October–December 2008**, 14–15.
3. Moorhead, J. S. Precision Guidance Kits (PGKs): Improving the Accuracy of Conventional Cannon Rounds. *Field Artillery* **January–February 2007**, 31–33.
4. Fresconi, F.; Brown, T.; Celmins, I.; DeSpirito, J.; Ilg, M.; Maley, J.; Magnotti, P.; Scanlan, A.; Stout, C.; Vazquez, E. Very Affordable Precision Projectile System and Flight Experiments. *Proceedings of the 27th Army Science Conference*, Orlando, FL, 2010.
5. Fresconi, F. E. Guidance and Control of a Projectile With Reduced Sensor and Actuator Requirements. *Journal of Guidance, Control, and Dynamics* **2011**, 34 (6), 1757–1766.
6. Habibi, S.; Roach, J.; Luecke, G. Inner-Loop Control for Electromechanical Flight Surface Actuation Systems. *Journal of Dynamic Systems, Measurement, and Control* **2008**, 130, 051002-1–051002-13.
7. Mani, S.; Sahjendra, S. N.; Parimi, S. K.; Yim, W. Adaptive Servoregulation of a Projectile Fin Using Piezoelectric Actuator. *Journal of Dynamic Systems, Measurement, and Control* **2007**, 129, 100–104.
8. Rabinovitch, O.; Vinson, J.; On the Design of Piezoelectric Smart Fins for Flight Vehicles. *Smart Materials and Structures* **2003**, 12, 686–695.
9. Mermagen, W. H. High-g Resistant Electronic Fuse for Projectile Payloads. *Journal of Spacecraft and Rockets* **1971**, 8 (8), 900–903.
10. Brown, T. G.; Davis, B.; Hepner, D.; Faust, J.; Myers, C.; Muller, P.; Harkins, T.; Hollis, M.; Miller, C.; Placzankis, B. Strap-Down Microelectromechanical (MEMS) Sensors for High-G Munition Applications. *IEEE Transactions on Magnetics* **2001**, 37 (1), 336–342.
11. DeSpirito, J.; Sifton, S.; Weinacht, P. Navier-Stokes Predictions of Dynamic Stability Derivatives: Evaluation of Steady-State Methods. *Journal of Spacecraft and Rockets* **2009**, 46 (6), 1142–1154.
12. Costello, M.; Sahu, J. Using Computational Fluid Dynamic/Rigid Body Dynamic Results to Generate Aerodynamic Models for Projectile Flight Simulation. *Journal of Aerospace Engineering* **2008**, 22 (G7), 1067–1079.

13. Sahu, J. Time-Accurate Numerical Prediction of Free-Flight Aerodynamics of a Finned Projectile. *Journal of Spacecraft and Rockets* **2008**, 45 (5), 946–954.
14. Weinacht, P. Projectile Performance, Stability, and Free-Flight Motion Prediction Using Computational Fluid Dynamics. *Journal of Spacecraft and Rockets* **2004**, 41 (2), 257–263.
15. Murphy, C. H. *Free Flight Motion of Symmetric Missiles*; report 1216; U.S. Army Ballistics Research Laboratory: Aberdeen Proving Ground, MD, July 1963.
16. McCoy, R. L. *Modern Exterior Ballistics*; Schiffer Publishing Ltd.: Atlen, PA, 1999.
17. Whyte, R. H.; Winchenbach, G. L.; Hathaway, W. H. Subsonic Free-Flight Data for a Complex Asymmetric Missile. *Journal of Guidance and Control* **1981**, 4 (1), 59–65.
18. Fresconi, F. E. Experimental Flight Characterization of Asymmetric and Maneuvering Projectiles From Elevated Gun Firings. *Journal of Spacecraft and Rockets*, accepted for publication, 2012.
19. Fresconi, F.; Celmins, I.; Fairfax, L. Optimal Parameters for Maneuverability of Affordable Precision Projectiles. *AIAA Aerospace Sciences Meeting*, Orlando, FL, January 2012.
20. Moore, F. G.; Moore, L. Y. Approximate Method to Calculate Nonlinear Rolling Moment due to Differential Fin Deflection. *Journal of Spacecraft and Rockets* **2012**, 49 (2), 250–260.
21. Wise, K. A.; Broy, D. J. Agile Missile Dynamics and Control. *Journal of Guidance Control, and Dynamics* **1998**, 21 (3), 441–449.
22. Pepitone, T. R.; Jacobson, I. D. Resonant Behaviour of a Symmetric Missile Having Roll Orientation-Dependent Aerodynamics. *Journal of Guidance and Control* **1978**, 1 (5), 335–339.
23. Nesline, F. W.; Wells, B. H.; Zarchan, P. Combined Optimal/Classic Approach to Robust Missile Autopilot Design. *Journal of Guidance, Control, and Dynamics* **1981**, 4 (3), 316–322.
24. Nesline, F. W.; Zarchan, P. Why Modern Controllers Can Go Unstable in Practice. *Journal of Guidance, Control, and Dynamics* **1984**, 7 (4), 495–500.
25. Ohta, H.; Kakinuma, M.; Nikiforuk, P. N. Use of Negative Weights in Linear Quadratic Regulator Synthesis. *Journal of Guidance* **1991**, 14 (4), 791–796.
26. Talole, S. E.; Godbole, A. A.; Kohle, J. P.; Phadke, S. B. Robust Roll Autopilot Design for Tactical Missiles. *Journal of Guidance, Control, and Dynamics* **2011**, 34 (1), 107–117.

27. Kang, S.; Kim, H. J.; Lee, J.; Jun, B.; Tahk, M. Roll-Pitch-Yaw Integrated Robust Autopilot Design for a High Angle-of-Attack Missile. *Journal of Guidance, Control, and Dynamics* **2009**, *32* (5), 1622–1628.
28. Arrow, A.; Williams, D. E. Comparison of Classical and Modern Missile Autopilot Techniques. *Journal of Guidance* **1989**, *12* (2), 220–227.
29. Williams, D. E.; Friedland, B.; Madiwale, A. N. Modern Control Theory for Design of Autopilots for Bank-to-Turn Missiles. *Journal of Guidance* **1987**, *10* (4), 378–386.
30. Maley, J. Roll Orientation from Commercial-Off-The-Shelf (COTS) Sensors in the Presence of Inductive Actuators. *Institute of Navigation Joint Navigation Conference*, Colorado Springs, CO, 2010.
31. Rogers, J.; Costello, M.; Hepner, D. Roll Orientation Estimator for Smart Projectiles Using Thermopile Sensors. *Journal of Guidance, Control, and Dynamics* **2011**, *34* (3), 688–697.
32. Rogers, J.; Costello, M.; Harkins, T.; Hamaoui, M. A Low-Cost Orientation Estimator for Smart Projectiles Using Magnetometers and Thermopiles. *Navigation* **2012**, *59* (1), 9–24.
33. Rogers, J.; Costello, M.; Harkins, T.; Hamaoui, M. Effective Use of Magnetometer Feedback for Smart Projectile Applications. *Navigation* **2011**, *58* (3), 203–219.
34. Arrow Tech Assoc. *PRODAS User Manual*; South Burlington, VT, 1997.

Nomenclature

$\phi, \dot{\phi}, \ddot{\phi}$	=	roll, roll rate, roll acceleration
I_{XX}	=	axial moment-of-inertia
m	=	mass
D	=	diameter
$S = \frac{\pi}{4} D^2$	=	reference area
V	=	velocity
M	=	Mach number
$\alpha, \beta, \bar{\alpha}, \phi_A$	=	pitch angle-of-attack, yaw angle-of-attack, total angle-of-attack, aerodynamic roll angle
ρ	=	atmospheric density
$\bar{q} = \frac{1}{2} \rho V^2$	=	dynamic pressure
C_{l_p}	=	roll damping moment coefficient
CP^R	=	radial center-of-pressure
CP^X	=	axial center-of-pressure
$C_N^C, C_{N\alpha}^C, C_{N\alpha^3}^C, C_{N\alpha^5}^C$	=	canard normal force coefficient, 1 st , 3 rd , and 5 th order terms
C_l	=	static roll moment coefficient
N	=	number
δ	=	deflection
$\vec{V}_{CG/I} = [u \ v \ w]^T$	=	velocity of projectile center-of-gravity
$\vec{\omega}_{B/I} = [p \ q \ r]^T$	=	angular velocity of projectile
$\vec{r}_{CG \rightarrow CP_i} = \begin{bmatrix} CP^X(M, \alpha_{C_i}) \\ CP^R(M, \alpha_{C_i}) \cos(\phi_{C_i}) \\ CP^R(M, \alpha_{C_i}) \sin(\phi_{C_i}) \end{bmatrix}$	=	vector from projectile center-of-gravity to center-of-pressure of i th lifting surface
\vec{T}_{BC_i}	=	
$= \begin{bmatrix} 1 & 0 & 0 \\ 0 & \cos(\phi_{C_i}) & \sin(\phi_{C_i}) \\ 0 & -\sin(\phi_{C_i}) & \cos(\phi_{C_i}) \end{bmatrix}$	=	transformation matrix from body frame to i th lifting surface frame
τ	=	time constant
\vec{x}, \vec{u}	=	state and controls vector
$\vec{A}, \vec{B}, \vec{F}$	=	system dynamics, controls, forcing function matrices
\vec{K}	=	gain matrix
\vec{R}, \vec{Q}	=	control error and control effort matrices
\vec{P}	=	Riccati equation matrix
t	=	time
L, F	=	roll moment, friction moment

subscripts

C	=	canard
F	=	fin
i	=	i^{th} lifting surface
CMD	=	command
D	=	delay
B	=	bias
R	=	random
μ	=	friction

NO. OF
COPIES ORGANIZATION

1 (PDF only) DEFENSE TECHNICAL INFORMATION CTR
DTIC OCA
8725 JOHN J KINGMAN RD
STE 0944
FORT BELVOIR VA 22060-6218

1 DIRECTOR
US ARMY RESEARCH LAB
IMAL HRA
2800 POWDER MILL RD
ADELPHI MD 20783-1197

1 DIRECTOR
US ARMY RESEARCH LAB
RDRL CIO LL
2800 POWDER MILL RD
ADELPHI MD 20783-1197

10 US ARMY ARDEC
RDAR MEF E
D CARLUCCI
M HOLLIS
C STOUT
A SANCHEZ
R HOOKE
J MURNANE
BLDG 94
PICATINNY ARSENAL NJ 07806-5000

8 US ARMY TACOM ARDEC
RDAR MEF S
D PANHORST
G MINER
N GRAY
R FULLERTON
B DEFRANCO
M MARSH
P FERLAZZO
D PASCUA
BLDG 94
PICATINNY ARSENAL NJ 07806-5000

3 US ARMY TACOM ARDEC
RDAR MEM C
R GORMAN
D CIMORELLI
K SANTANGELO
BLDG 94
PICATINNY ARSENAL NJ 07806-5000

NO. OF
COPIES ORGANIZATION

2 US ARMY ARDEC
RDAR MEM C
D DEMELLA
A LICHTENBERG-SCANLAN
BLDG 94
PICATINNY ARSENAL NJ 07806-5000

2 US ARMY TACOM ARDEC
RDAR MEM M
C MOEHRINGER
J TRAVAILLE
BLDG 94
PICATINNY ARSENAL NJ 07806-5000

1 US ARMY TACOM ARDEC
AMSRD AAR AEPS
J ROMANO
BLDG 407
PICATINNY ARSENAL NJ 07806-5000

4 US ARMY TACOM ARDEC
RDAR MEM A
E VAZQUEZ
G MALEJKO
W KOENIG
S CHUNG
BLDG 94S
PICATINNY ARSENAL NJ 07806-5000

2 RDECOM ARDEC
RDAR MEM A
J GRAU
W TOLEDO
BLDG 94
PICATINNY ARSENAL NJ 07806-5000

3 US ARMY TACOM ARDEC
RDAR MEF I
R GRANITZKI
J CHOI
L VO
BLDG 95
PICATINNY ARSENAL NJ 07806

1 US ARMY ARDEC
RDAR MEM C
M LUCIANO
BLDG 65S
PICATINNY ARSENAL NJ 07806

NO. OF
COPIES ORGANIZATION

1 US ARMY TACOM ARDEC
RDAR MEE W
J LONGCORE
BLDG 382
PICATINNY ARSENAL NJ 07806

1 US ARMY ARDEC
RDAR MEF
M HOHIL
BLDG 407
PICATINNY ARSENAL NJ 07806-5000

4 RDECOM ARDEC
AMSRD AMR SG SD
J BAUMAN
H SAGE
S DUNBAR
B NOURSE
BLDG 5400
REDSTONE ARSENAL AL 35898

1 US ARMY ARMAMENT RD&E CTR
RDAR MEM C
D NGUYEN
BLDG 94
PICATINNY ARSENAL NJ 07806-5000

1 RDECOM AMRDEC
RDMR WDG N
B GRANTHAM
BLDG 5400
REDSTONE ARSENAL AL 35898

2 PM CAS
SFAE AMO CAS
R KIEBLER
P MANZ
BLDG 171
PICATINNY ARSENAL NJ 07806

2 PM CAS
SFAE AMO CAS EX
J MINUS
M BURKE
BLDG 171
PICATINNY ARSENAL NJ 07806

1 US ARMY TACOM ARDEC
SFAE AMO MAS
C GRASSANO
BLDG 354
PICATINNY ARSENAL NJ 07806

NO. OF
COPIES ORGANIZATION

3 US ARMY ARDEC
SFAE AMO CAS MS
P BURKE
G SCHWARTZ
J HILT
BLDG 162 S
PICATINNY ARSENAL NJ 07806-5000

1 US ARMY ARDEC
SMO MAS LC
D RIGOGLIOSO
BLDG 354
PICATINNY ARSENAL NJ 07806

1 PM MAS
SFAE AMO MAS SETI
J FOULTZ
BLDG 354
PICATINNY ARSENAL NJ 07806

1 FIRES DEPUTY MGR
EXP MANEUVER WARFARE
OFC OF NAVAL RSRCH
ONR 30
875 N RANDOLPH ST
RM 1155B
ARLINGTON VA 22203

1 US ARMY TACOM ARDEC
RDAR MEF E
T RECCHIA
BLDG 94
PICATINNY ARSENAL NJ 07806-5000

2 NVL SURFC WARFARE CTR
DAHLGREN DIVISION
N COOK
L STEELMAN
G33
6210 TISDALE RD STE 223
DAHLGREN VA 22448-5114

2 ATK ADVANCED WEAPONS DIV
R DOHRN MN07 MN07 MN14
J WEYRAUCH
4700 NATHAN LANE N
PLYMOUTH, MN 554422

1 SAIC
D HALL
1150 FIRST AVE STE 400
KING OF PRUSSIA PA 19406

NO. OF
COPIES ORGANIZATION

1 ALLIANT TECHSYSTEMS INC
ALLEGANY BALLISTICS LAB
S OWENS
MS WV01 08 BLDG 300 RM 180
210 STATE RTE 956
ROCKET CTR WV 26726-3548

1 GEN DYNAMICS ST MARKS
H RAINES
PO BOX 222
SAINT MARKS FL 32355-0222

3 GOODRICH SENS AND INERTIAL SYS
T KELLY
P FRANZ
S ROUEN
100 PANTON RD
VERGENNES VT 05491

1 US ARMY ARDEC
RDAR MEM C
P MAGNOTTI
BLDG 94
PICATINNY ARSENAL NJ 07806

5 BAE ARM SYS DIV
T MELODY
J DYVIK
P JANKE
B GOODELL
O QUORTRUP
4800 E RIVER RD
MINNEAPOLIS MN 55421-1498

1 US ARMY YUMA PROVING GROUND
TEDT YPY MW
M BARRON
301 C STREET
YUMA AZ 85365-9498

1 TRAX INTRNTL CORP
R GIVEN
US ARMY YUMA PROVING GROUND
BLDG 2333
YUMA AZ 85365

1 ARROW TECH ASSOC
W HATHAWAY
1233 SHELBURNE RD
STE D-8
SOUTH BULINGTON VT 05403

NO. OF
COPIES ORGANIZATION

1 GEORGIA INST OF TECHLGY
SCHOOL OF AEROSPACE ENG
M COSTELLO
ATLANTA GA 30332

1 TEXAS A&M
SCHOOL OF AEROSPACE ENG
J ROGERS
COLLEGE STATION TX 77843

1 ROSE-HULMAN INST OF TECHLGY
SCHOOL OF MECHANICAL ENG
B BURCHETT
TERRE HAUTE IN 47803

ABERDEEN PROVING GROUND

5 COMMANDER
US ARMY TACOM ARDEC
AMSRD AR AEF D
J MATTS
A SOWA
J FONNER
M ANDRIOLO
B NARIZZANO
B 305
APG MD 21005

45 DIR USARL
RDRL WM
P PLOSTINS
RDRL WML
P PEREGINO
M ZOLTOSKI
RDRL WML A
W OBERLE
R PEARSON
L STROHM
RDRL WML D
M NUSCA
J SCHMIDT
RDRL WML E
V BHAGWANDIN
I CELMINS
G COOPER
J DESPIRITO
L FAIRFAX
F FRESCONI (5 CPS)
J GARNER
B GUIDOS
K HEAVEY
G OBERLIN

NO. OF
COPIES ORGANIZATION

J SAHU
S SILTON
P WEINACHT
RDRL WML F
B ALLIK
T BROWN
B DAVIS
T HARKINS
M ILG
G KATULKA
D LYON
J MALEY
C MILLER
P MULLER
D PETRICK
B TOPPER
RDRL WML G
J BENDER
W DRYSDALE
M MINNICINO
RDRL WML H
M FERREN-COKER
J NEWILL
R SUMMERS
RDRL WMP F
R BITTING
N GNIAZDOWSKI